RESEARCH ARTICLE

Key Points:
- CIR and CME were studied as they propagate through the inner solar system
- They merge beyond Mars and later compress the Saturn magnetosphere
- The ENLIL-predicted CME arrival times are more accurate than the CIR times

Supporting Information:
- Readme
- Movie S3
- Movie S2
- Movie S1

Correspondence to:
A. J. Prise,
ailsa.prise.11@ucl.ac.uk

Analysis of a coronal mass ejection and corotating interaction region as they travel from the Sun passing Venus, Earth, Mars, and Saturn

A. J. Prise[1], L. K. Harra[1], S. A. Matthews[1], C. S. Arridge[2], and N. Achilleos[3]

[1]Department of Space and Climate Physics, Mullard Space Science Laboratory, University College London, Dorking, UK, [2]Department of Physics, Lancaster University, Lancaster, UK, [3]Centre for Planetary Sciences at UCL/Birkbeck, London, UK

Abstract During June 2010 a good alignment in the solar system between Venus, STEREO-B, Mars, and Saturn provided an excellent opportunity to study the propagation of a coronal mass ejection (CME) and closely occurring corotating interaction region (CIR) from the Sun to Saturn. The CME erupted from the Sun at 01:30 UT on 20 June 2010,with $v \approx 600$ km s^{-1}, as observed by STEREO-B, Solar Dynamics Observatory, and SOHO/Large Angle and Spectrometric Coronagraph. It arrived at Venus over 2 days later, some 3.5 days after a CIR is also detected here. The CIR was also observed at STEREO-B and Mars, prior to the arrival of the CME. The CME is not directed earthward, but the CIR is detected here less than 2 days after its arrival at Mars. Around a month later, a strong compression of the Saturn magnetosphere is observed by Cassini, consistent with the scenario that the CME and CIR have merged into a single solar transient. The arrival times of both the CME and the CIR at different locations were predicted using the ENLIL solar wind model. The arrival time of the CME at Venus, STEREO-B, and Mars is predicted to within 20 h of its actual detection, but the predictions for the CIR showed greater differences from observations, all over 1.5 days early. More accurate predictions for the CIR were found by extrapolating the travel time between different locations using the arrival times and speeds detected by STEREO-B and ACE. We discuss the implications of these results for understanding the propagation of solar transients.

1. Introduction

Current spacecraft are located at all planets in the inner solar system, at three different points at 1 AU, and at Saturn, allowing for the opportunity to study the impact of distinct solar transients on more than one location. Analyzing a solar wind disturbance by observing it throughout the inner and outer solar system also provides the opportunity to study the characteristics of its propagation and learn more about its evolution as it travels through the solar system. Solar wind transients can be interplanetary coronal mass ejections (ICMEs) or corotating interaction regions (CIRs).

CIRs are formed when a region of fast solar wind catches up with a region of slow solar wind creating a density enhancement at the interface between them, known as a stream interaction region (SIR). The average duration of this interaction region at 1 AU is 36.7 ± 0.9 h, with a size of 0.41 ± 0.01 AU [*Jian et al.*, 2006]. There will be a compression region ahead of this interface and a rarefaction region behind. Pairs of shocks may also form at the edges of the interaction region, particularly at higher heliocentric distances, beyond $\approx$3 AU, as the compression wave steepens [*Gosling and Pizzo*, 1999; *Gosling et al.*, 1976; *Hundhausen and Gosling*, 1976; *Smith and Wolfe*, 1976]. The fast solar wind originates from coronal holes that become more frequent at lower solar latitudes during the declining phase of the solar cycle. These high-speed streams of solar wind, and therefore the associated interaction region, rotate with the Sun, sweeping out large areas of longitude. If they persist for multiple solar rotations, they become known as CIRs [*Gosling and Pizzo*, 1999]. A CIR has an average duration at 1 AU of 36.8 ± 1.2 h and a size of 0.44 ± 0.02 AU [*Jian et al.*, 2006]. They can be observed in situ as an increase and then decrease in density, an increase in solar wind velocity, entropy and proton temperature, velocity deflections, a pileup of total pressure and a compression of the magnetic field [*Jian et al.*, 2006, 2008]. The presence of at least five of these signatures is required for a CIR to be strongly identified. Many CIRs have a sharp stream interface, which is the actual interface boundary between fast and slow solar wind streams and is defined as the peak in total pressure, usually accompanied by the increase in velocity and temperature and a drop in density following the compression [*Jian et al.*, 2006]. The CIRs have also been extensively modeled and compared with observations, for

example, using ENLIL [e.g., *Jian et al.*, 2011; *Odstrcil and Pizzo*, 2009]. *Wood et al.* [2010] construct a 3-D model of a CIR and generate synthetic whitelight images that successfully reproduce its general appearance and evolution in the Heliospheric Imagers, HI2, on the STEREO (Solar TErrestrial RElations Observatory) spacecraft. They note that the curvature of the CIR is compatible with the observed slow solar wind speed. As CIRs can be very long lived structures in the heliosphere and have the potential to influence vast areas of it, their propagation through the solar system is important to study.

ICMEs are the interplanetary counterparts of CMEs and occur more frequently during solar maximum. In comparison to CIRs, they are short-lived solar transients, passing through the solar system with speeds of up to 2500 km s^{-1}, but often cause stronger impacts on planets. ICMEs can consist of several different regions observed in the solar wind including a shock, plasma sheath, solar wind pileup, ejecta, compression regions, and driver gas [*Rouillard*, 2011]. These different structures can be observed in situ by a variety of indicators lasting 1–2 days, including decreases in proton temperature, an enhancement of total pressure, declining solar wind speed, an enhanced α/proton ratio, low plasma β, and counterstreaming suprathermal electrons (see review by *Zurbuchen and Richardson* [2006]). A particular subset of ICME ejecta is magnetic clouds, which are characterized by the smooth rotation of the magnetic field, an overall enhancement of the magnetic field, and often a low plasma beta or proton temperature [*Klein and Burlaga*, 1982].

There have been several studies tracking solar transients through the inner solar system, using multipoint remote and in situ observations to constrain the characteristics of the transients and learn more about their propagation. *Rouillard et al.* [2009] observe a complex solar storm consisting of multiple solar transients and track it from the Sun to Venus. The main ICME is observed as two parts by SECCHI, the Sun-Earth Connection Coronal and Heliospheric Investigation, on STEREO-A, with in situ measurements by Venus Express (VEx) and MErcury Surface, Space ENvironment, GEochemistry and Ranging (MESSENGER) confirming the presence of a flux rope within them. Multiple CMEs were observed by *Möstl et al.* [2012], making use of observations from many spacecraft including VEx, MESSENGER, STEREO, and ACE. They demonstrate that multipoint observations are sometimes the only way to gain a clear picture of a complex sequence of events. *Nieves-Chinchilla et al.* [2013] also utilize multipoint observations to analyze the evolution of a "stealth" CME, which is deflected by several nearby coronal holes. Remote observations from STEREO, the Solar and Heliospheric Observatory (SOHO), and the Solar Dynamics Observatory (SDO) are used in tandem with in situ measurements at Wind, ACE (the Advanced Composition Explorer), and MESSENGER. *Williams et al.* [2011] track multiple CIRs through the inner solar system, observing them with STEREO, Mars Express, Venus Express, and ACE spacecraft. They use these multipoint observations to assess methods to predict the arrival of CIRs at Venus, Mars, and the STEREO spacecraft. They find that their method, which extrapolates the CIR arrival at other locations using its speed and arrival at ACE, predicts arrival times better than an alternative method using STEREO Heliospheric Imagers.

Studies of propagation to the outer heliosphere have been much less frequent. One of the only studies to track an ICME to the outer solar system was carried out by *Prangé et al.* [2004]. They combined remote sensing of the Sun, Jupiter, and Saturn with in situ observations of the Earth to track the propagation of an ICME from its eruption to the initiation of auroral storms on the outer planets, showing that shocks retain their ability to drive aurora throughout the solar system. Since then, several CIRs have been observed in the outer solar system, such as those detected by Cassini on its approach to Saturn in late 2003/2004 [*Jackman et al.*, 2004, 2008]. They also observe this highly structured solar wind being disrupted by ICMEs in November 2003 as a result of the Halloween storms, concluding that shocks can excite significant magnetospheric dynamics at Saturn. During the Cassini orbit insertion at Saturn, *Jackman et al.* [2005] and *Achilleos et al.* [2006] observe the arrival of a CIR at Saturn, and the resulting compression of the magnetosphere leading to reconnection in the magnetotail. Beyond Saturn, *Liu et al.* [2014] study a series of CMEs which are observed near the Earth and then modeled further out. These structures merge together and the model predicts their arrival at 120 AU, which is seen to correspond to a period of radio emissions and disturbance of galactic cosmic rays as observed by Voyager 1.

When CIRs and ICMEs interact, they can form merged interaction regions (MIRs), regions where total solar wind pressure is enhanced, formed by multiple solar transients. Multiple ICMEs propagating at different speeds can catch up with one another as they travel and also merge to form MIRs. The resulting structure can strongly influence geomagnetic activity at the Earth [*Rouillard et al.*, 2010]; for example, if an ICME interacts with a CIR or an earlier, slower ICME, this can cause a compression, resulting in an intensification of

the magnetic field. This would be a particular issue if the constituent ICMEs contain magnetic clouds with a highly ordered magnetic field [*Xiong et al.*, 2007; *Wang et al.*, 2003, 2005]. MIRs can be very complex and require multiple observations to verify how they have formed and what their structure is [*Rouillard et al.*, 2010; *Burlaga et al.*, 2003].

The interaction of multiple ICMEs with each other has attracted significant study. The hybrid code HAFv.2+3DMHD is used to model the interactions of several ICMEs by *Wu et al.* [2007, 2014], demonstrating that the model can help link ICMEs and shocks observed at 1 AU to their solar source. *Wu et al.* [2012] use this model to simulate multiple ICMEs, observing several instances of the ICMEs merging, and also note the leading edges of many ICMEs are asymmetric or distorted due to interactions with the background solar wind. *Wu et al.* [2011] model a single CME which propagates with a highly asymmetric shape due to its interaction with the background solar wind and the presence of a high-speed solar wind stream. The interaction of two specific ICMEs were modeled by *Lugaz et al.* [2009] and *Webb et al.* [2009]. *Lugaz et al.* [2009] conclude that the second, fast ICME catches up with the earlier, slower ICME and decelerates before merging with it. *Webb et al.* [2009] compare the results of four different models, including ENLIL and HAFv.2 and find that they generally all agree on the events' appearance and kinematic evolution. They suggest, however, that the ICMEs may not have merged but instead only partially interacted or the second ICME simply overtook the first. It has also been observed that interacting ICMEs can lead to significant changes to the direction of propagation of the transients, sometimes resulting in strong deflections [*Lugaz et al.*, 2012]. *Shen et al.* [2012] also observe the strong deflection of two ICMEs and suggest that the collision could be superelastic, which they then validate with simulations [*Shen et al.*, 2013].

CME deflections are also observed as a result of interactions with the background solar wind and outer corona. Equatorward deflections of CMEs were first reported by *MacQueen et al.* [1986] near solar minimum and further reported by, e.g., *Gopalswamy et al.* [2003], *Cremades and Bothmer* [2004], and *Wang et al.* [2011]. This systematic deflection is due to the dominance of large-scale dipolar magnetic field and flow at solar minimum, in comparison to much less ordered conditions during solar maximum. *Gui et al.* [2011] verify that CME deflections in the inner corona are consistent in strength and direction with the gradient of magnetic energy density. However, as the density of magnetic field decreases with heliocentric distance, this effect should only be significant close to the Sun. *Isavnin et al.* [2014] find that 60% of the latitudinal deflection occurs below 30 R_{Sun}, suggesting that interactions with coronal holes may be the main cause of this deflection. Longitudinal deflections of ICMEs in interplanetary space are observed by *Wang et al.* [2004] as a result of ICME interactions with the Parker spiral. Faster ICMEs are blocked by the slow solar wind ahead and deflected eastward, whereas slower ICMEs are accelerated by faster solar wind behind and deflected westward. *Wang et al.* [2014] model a specific ICME and conclude that the deflection is due to the interaction of the ICME with the solar wind, rather than the gradient of the magnetic energy density which is the cause of deflection in the corona. Like *Nieves-Chinchilla et al.* [2013], *Wood et al.* [2012] observe a CME being deflected by nearby coronal holes. However, in this instance, only the ejecta is deflected, not the shock. Part of the shock expands more rapidly into the high-speed wind stream from the coronal hole and arrives at STEREO-A a day before the rest of the shock, traveling in normal solar wind, arrives at the Earth.

In this study, we make use of multiple remote and in situ observations sampling the inner and outer solar system to track two different solar transients. We observe a CME erupting from the Sun and track it through the inner solar system, where it is observed in situ at Venus, STEREO-B, and Mars. A CIR propagating ahead of the CME is observed in these three locations, as well as at Earth. We make use of the ENLIL prediction model to estimate the time of arrival of both CIR and ICME and compare with the in situ data to make an estimate of the accuracy through the solar system. ENLIL results indicate that the ICME catches up with the CIR and merges with it. A strong magnetospheric compression that is consistent with this scenario is subsequently observed at Saturn.

2. Instrumentation and Prediction Model

For this study, data were utilized from multiple spacecraft and instruments, to build up a complete picture of the CME and CIR as they travel through the solar system. The CME was observed directly by the SECCHI [*Howard et al.*, 2008] instrument suite on STEREO. The CME eruption was observed on-disk by the Extreme Ultraviolet Imager (EUVI) [*Wuelser et al.*, 2004] and propagating away from the Sun by the Cor-1 and Cor-2 [*Thompson et al.*, 2003] coronagraphs and the Heliospheric Imagers (HI) [*Eyles et al.*, 2009]. From the Earth,

the CME was imaged on-disk by the Atmospheric Imaging Assembly (AIA) [*Lemen et al.*, 2012] on SDO and off the Sun with the Large Angle and Spectrometric Coronagraph (LASCO) [*Brueckner et al.*, 1995] experiment on SOHO [*Domingo et al.*, 1995]. The ICME and CIR were observed in situ at multiple locations throughout the solar system. The CIR was detected in situ at the Earth by the Solar Wind Electron Proton Alpha Monitor (SWEPAM) [*McComas et al.*, 1998] onboard ACE. In situ measurements were taken at STEREO-B using the magnetometer of the In situ Measurements of Particles and CME Transients (IMPACT) [*Luhmann et al.*, 2008] suite of instruments and the Plasma and Suprathermal Ion Composition (PLASTIC) investigation [*Galvin et al.*, 2008]. At Mars and Venus, in situ measurements are presented from the Electron Sensor (ELS) of the Analyzer of Space Plasmas and Energetic Atoms 3 and 4 (ASPERA-3 [*Barabash et al.*, 2006] and ASPERA-4 [*Barabash et al.*, 2007]) instruments on board the Mars Express (MEx) and Venus Express, respectively. In addition to ASPERA-4, VEx also carries a Fluxgate Magnetometer [*Zhang et al.*, 2006], which was also used to identify the arrival of the CME and CIR. Both Venus Express and Mars Express have highly elliptical orbits, spending a short time within the exosphere of the planet. Venus Express completes roughly one orbit per day, with ASPERA-4 operational for several hours at periapsis and apoapsis only, while the magnetometer runs continuously. Mars Express completes three to four orbits per day, with ASPERA-3 running for several hours around periapsis only. At Saturn, the Cassini spacecraft provides in situ measurements of the magnetosphere with the magnetometer (MAG) [*Dougherty et al.*, 2004] and Cassini Plasma Spectrometer (CAPS) [*Young et al.*, 2004].

The arrival of these events was predicted throughout the solar system using the ENLIL + cone model [*Odstrcil and Pizzo*, 1999; *Odstrcil et al.*, 2004]. ENLIL is a 3-D time-dependent MHD forecast model of the solar wind, available from the Community Coordinated Modeling Center (CCMC) at NASA Goddard Space Flight Center. The addition of the cone model allows the simulation of up to five ICMEs propagating through the solar system. ENLIL+cone is used by both NOAA and the UK Met Office to provide predictions for the arrival of ICMEs at the Earth for real-time space weather forecasting. A simulation run of ENLIL will span one Carrington rotation and can run to 2 AU (encompassing the orbit of Mars) or 10 AU (encompassing the orbit of Saturn). For these runs, ENLIL takes an input at its inner boundary of 21.5 R_{Sun} from the Wang-Sheely-Arge (WSA [*Arge and Pizzo*, 2000]) model or the Magnetohydrodynamics Around a Sphere (MAS [*Riley et al.*, 2006]). The MAS model is a full 3-D MHD model, but the WSA model requires an input from a current sheet model and a magnetostatic potential field source surface (PFSS) model [*Schatten et al.*, 1969]. These can take synoptic magnetograms from several different observatories. For this study, the WSA input to ENLIL was used, with the magnetogram from the Mount Wilson Observatory.

The cone model requires several input parameters to simulate the ICME, including the CME width, latitude, longitude, speed, and time it arrives at 21.5 R_{Sun} (the inner boundary of the model). The CME Analysis Tool, available from the CCMC website, utilizes the images of the CME in coronagraphs from multiple viewpoints to constrain the input parameters. These input parameters are then used by ENLIL to introduce an over pressured plasma cloud into the ambient solar wind, corresponding to the ICME. This plasma cloud does not incorporate the internal magnetic signal of the ICME, however, which is one of its most significant parameters. This means that ENLIL cannot model the flux rope structure of a ICME, so the simulated evolution of the ICME ejecta is not accurate. However, the propagation of any associated density enhancements, such as plasma sheath regions, shocks, solar wind pileup, or compression regions, is not affected by this. Although these regions cannot be specifically distinguished in the simulation, it can still provide a valid estimate of the arrival of the associated solar wind disturbance at different locations in the solar system. In this study, we use the term "ICME" to refer to the entire solar wind region altered by the CME transient, as defined by *Rouillard* [2011] including any shock, sheath, solar wind pileup, and ejecta regions. We therefore refer to the solar wind disturbance as simulated by ENLIL as an ICME, along with the structures identified in observations. The different regions of the ICME such as shock, solar wind pileup, and ejecta are explicitly stated when we are referring to them.

Multiple studies have been made of the performance of ENLIL, comparing its predictions with in situ observations and alternative model results. Recent studies include those by *Vršnak et al.* [2014] which compares the ENLIL+cone model with the analytical drag-based model, finding that the differences in the simulated and observed arrival times for ICMEs at L1 are similar for both models, at around 14 h. *Falkenberg et al.* [2010] simulate a single ICME event multiple times, changing different ENLIL input parameters from the default values. They note that despite ENLIL being unable to simulate the internal magnetic structure of the ICME, the magnitude of the initial signal, arrival time, and dynamic pressure of the event is still well

reproduced at L1. *Taktakishvili et al.* [2009] assess the performance of ENLIL simulating 14 ICME events, comparing their shock arrival times to a mean velocity and empirical shock arrival model. They find that ENLIL generally performs better than the reference models, with an average error of 6 h. A number of studies make use of ENLIL results at locations other than L1. In particular, *Baker et al.* [2009, 2011, 2013] use ENLIL simulations to provide context for MESSENGER observations at Mercury, as the plasma instrument onboard cannot always adequately sample the solar wind distribution functions. *Falkenberg et al.* [2011a] study several ICMEs and use GOES data at Earth and Mars Global Surveyor (MGS) data at Mars to evaluate the performance of ENLIL predictions. They find that the multipoint observations are crucial to validate the models, as two different ICMEs can seem very similar when observed at only one location. They also note that possible deflections of the ICME will increase uncertainty in the simulation, as this is less likely to be correctly modeled without the internal magnetic structure of the ICME. *Falkenberg et al.* [2011b] was a follow up to this study, which again uses in situ observations of ICMEs at Earth and Mars to evaluate ENLIL predictions. They find that shocks can arrive almost simultaneously at Mars and Earth due to the presence of a high-speed stream, allowing part of the CME shock front to travel faster than the rest. In addition to several studies that use ENLIL+cone to predict the arrival of ICMEs at Earth, the ability of ENLIL to reproduce the background solar wind has also been analyzed. *Jian et al.* [2011], *Broiles et al.* [2013], and *Lee et al.* [2009] compare the performance of WSA/ENLIL and MAS/ENLIL to simulate the background solar wind and find that in general, both versions are capable of reproducing the large-scale structure of the solar wind but find that the timing can be off by 1–2 days. *MacNeice et al.* [2011] validates community models and assesses the accuracy of WSA/ENLIL in tracing field lines through the heliosphere. They find that the average error in the position of the foot points of field lines is roughly 20°, which could correspond to timing errors of 1–2 days for structures in the ambient solar wind. The simulated values of solar wind parameters also show discrepancies with observations. For example, both *Jian et al.* [2011] and *Broiles et al.* [2013] find that ENLIL significantly underestimates the magnetic field strength and total pressure. *Jian et al.* [2011] also find that the ENLIL simulations underestimate the temperature and that this is more extreme at 5.4 AU than 1 AU. However, the simulated density peaks were generally 2–4 times greater than observations for the SIRs studied by *Jian et al.* [2011], though *Lee et al.* [2009] find that in general, WSA/ENLIL yields densities similar to the observations at ENLIL. *Gressl et al.* [2014] also compare the MAS/MAS model with these two versions of ENLIL and find similar results, again with uncertainties in the time of arrival of a high-speed stream of about 1 day.

3. Observations

3.1. Remote Observations

The CME was observed erupting at 01:30 UT on 20 June 2010, on the solar disk by STEREO-B (at roughly N30E90), as seen in Figure 1, and also on the eastern limb by SDO. The CME was seen clearly off the eastern limb in the SOHO/LASCO and the STEREO-A/Cor-2 coronagraphs, as shown in Figure 2. At this time, STEREO-B was 70° behind the Earth and STEREO-A was 74° ahead (see Figure 3). From this we can conclude that the CME was directed roughly toward STEREO-B, although it is not visible as a halo CME in STEREO-B coronagraphs. Height-time plots of LASCO coronagraph observations give this CME a radial speed of 591 km s^{-1}.

As the ICME is directed toward STEREO-B, it is not observed by HI-B; however, it is seen by HI-1A and HI-2A, shown in Movies S1 and S2 (in the supporting information). It enters the field of view of HI-1A at around 00:49 UT on 21 June and passes over Venus early on 22 June 2010, seen in Movie S1. The ICME enters the field of view of HI-2A at around 08:09 UT 22 June, seen in Movie S2. LASCO C2 observations showed this CME passing by an earlier, slower CME which is also directed roughly toward STEREO-B but further southward (see Movie S3 in the supporting information). In HI-1A observations it is clear that this ICME is directed far enough below the ecliptic plane that it will not hit any planets and therefore is unlikely to add further complexity to the scenario. It is observed entering the field of view of HI-1A at roughly 15:29 UT 22 June and passes below Venus at roughly 08:49 UT 23 June (Movie S1).

The source of the high-speed stream associated with the CIR is a recurrent low-latitude coronal hole, shown in Figure 1. It is visible on the solar disk as seen from SDO for several days and is roughly central on 23 June 2010.
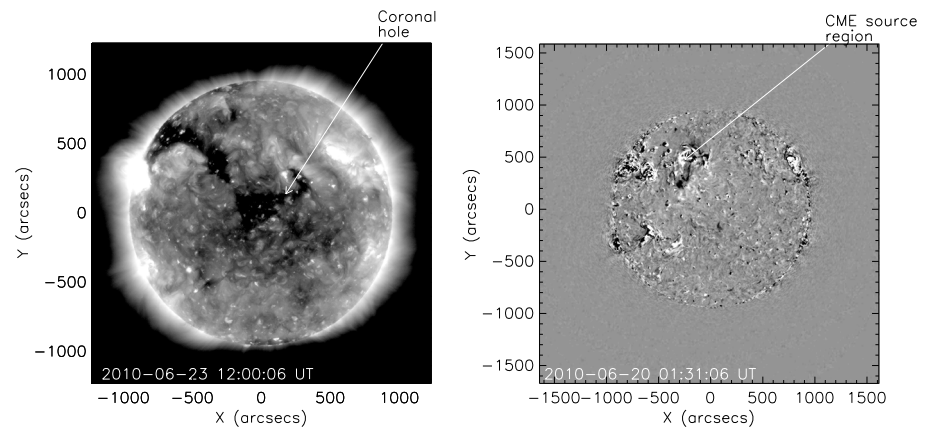
Figure 1. (left) AIA/SDO image of the solar disk on 23 June 2010 in the 193 Å passband. The coronal hole labeled is the source of the high-speed solar wind stream which causes the CIR. (right) Running difference EUVI-B image at 01:30 UT showing the CME source location.

3.2. ENLIL Prediction Modeling

The arrival times of the ICME throughout the solar system were predicted using the ENLIL+cone model, described above. The input parameters used were obtained from the CME Analysis Tool and included a longitude of E84°, a CME width of 27° and a velocity of 628 km s^{-1}, which agrees fairly well with the direction and speed of the CME found above.

The ENLIL run of the inner solar system (out to 2 AU) for this ICME shows that it clearly impacts Venus, STEREO-B, and Mars, as shown in Figure 4. From this the CIR can also be seen passing through prior to the ICME.
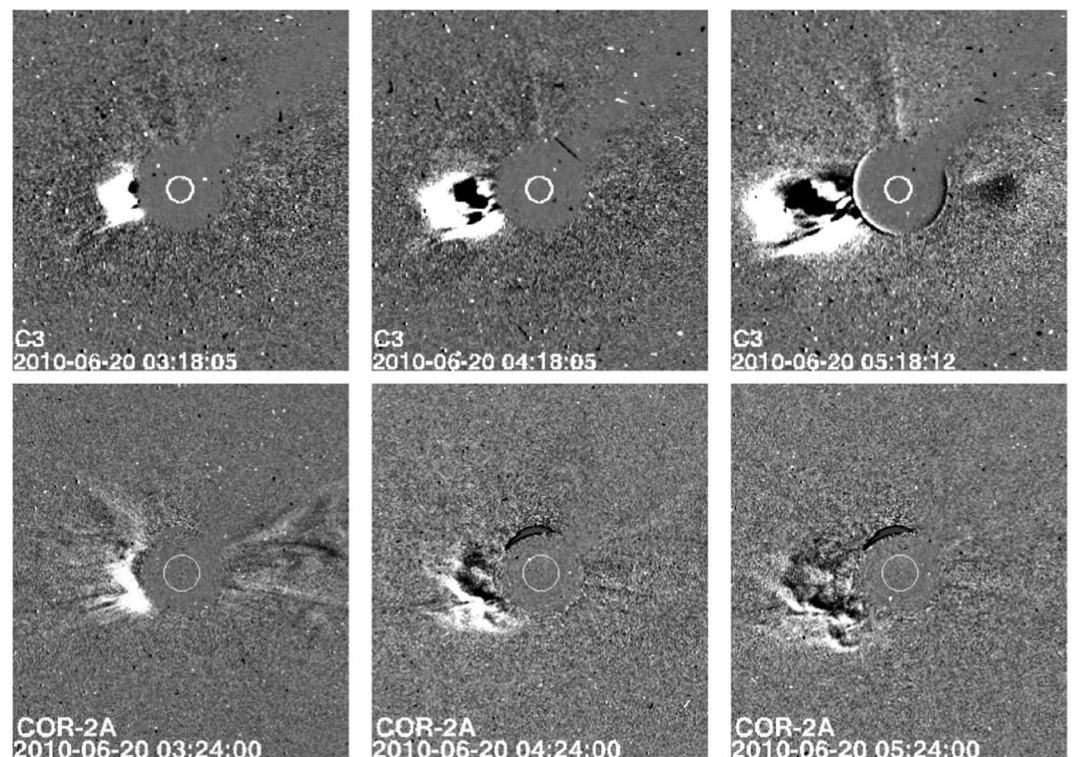

Figure 2. Running difference images from (top row) C3 and (bottom row) Cor2-A coronagraphs, showing the eruption of the CME.
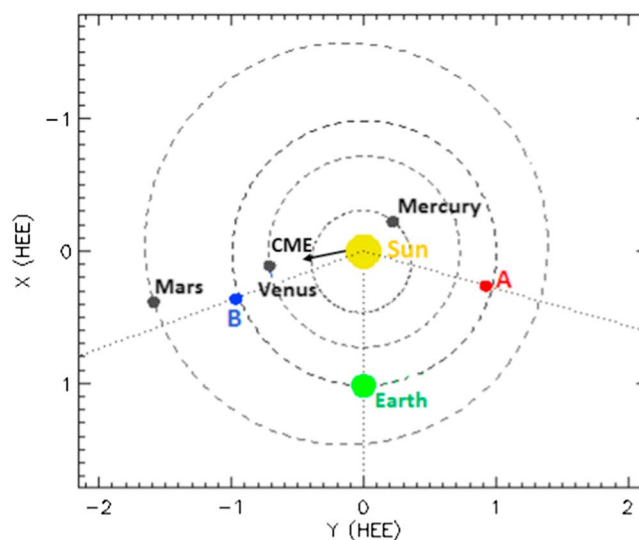
Figure 3. Positions of the inner solar system planets and both STEREO spacecraft on 20 June 2010. The direction of the erupting CME is indicated by the black arrow. http://stereo-ssc.nascom.nasa.gov/cgi-bin/make_where_gif
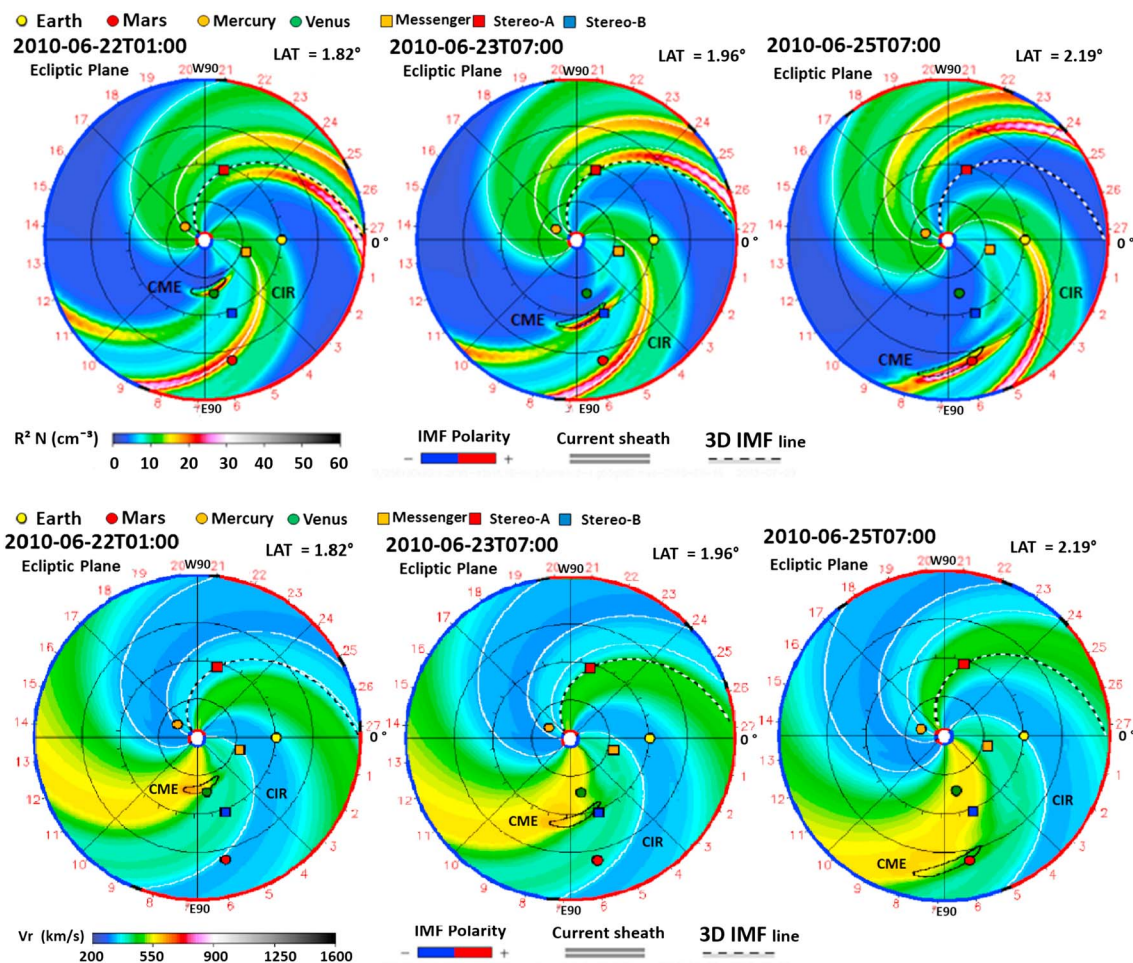

Figure 4. Ecliptic view of the modeled (top rows) solar wind density and (bottom rows) solar wind velocity at three different time steps, indicating the CME arrival at Venus, STEREO-B, and Mars. The scales for the density and velocity are given by the color bars. The locations of Venus, STEREO-B, Mars, and other planets and spacecraft are indicated by the colored symbols.
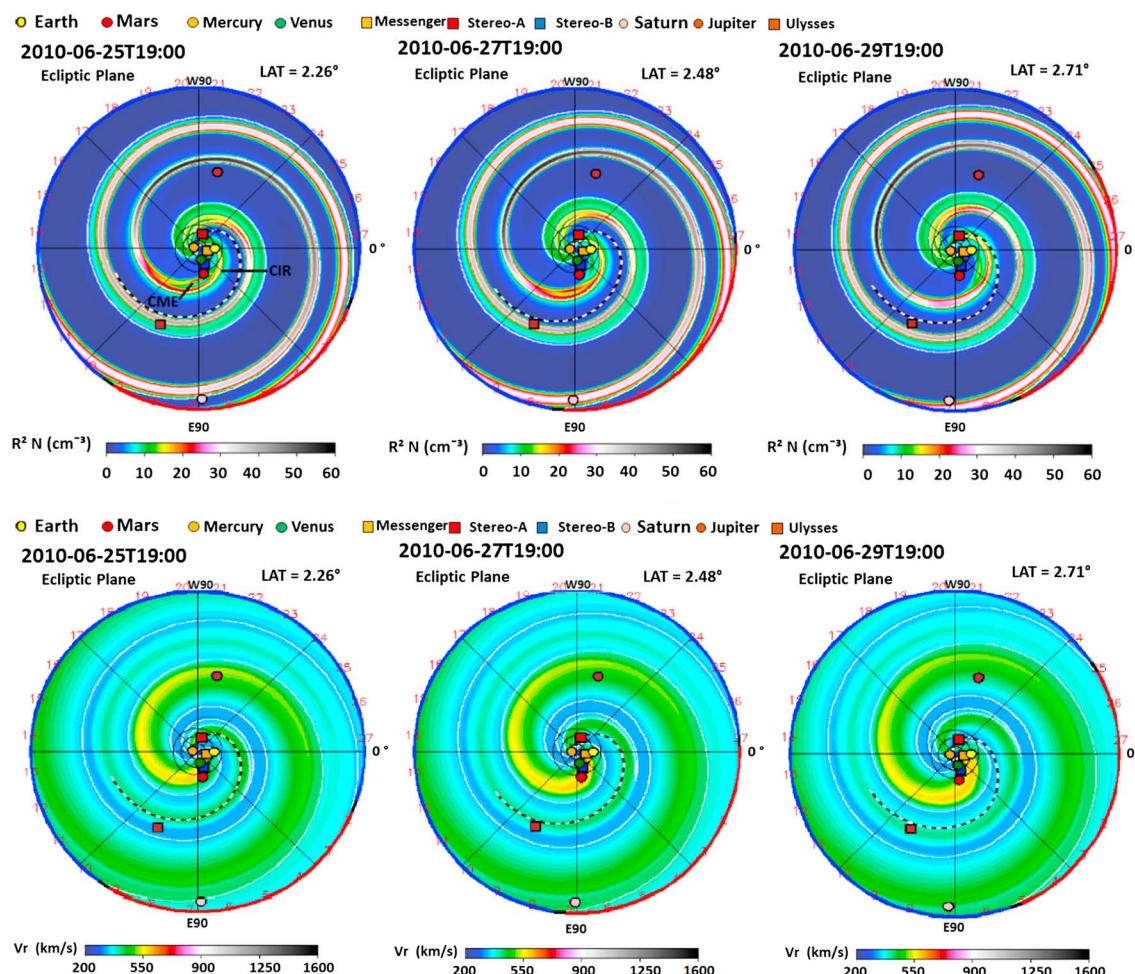
Figure 5. Ecliptic view of the modeled (top rows) solar wind density and (bottom rows) solar wind velocity at three different time steps, showing the CME as it merges with the CIR beyond the orbit of Mars. The scales for the density and velocity are given by the color bars. The locations of Venus, STEREO-B, Mars, and other planets and spacecraft are indicated by the colored symbols.

An ENLIL run of the same ICME in the outer solar system (out to 10 AU) does not show it impacting any of the outer planets. Instead, it indicates that the ICME merges with the preceding CIR, beyond the orbit of Mars, and as such does not reach Saturn as an ICME, despite its favorable position (see Figure 5). The simulated CIR is predicted to impact Saturn roughly 1 month later.

3.3. The CIR and ICME at Venus

Both the CIR and the ICME are observed in situ at Venus. As Venus Express carries a magnetometer which is continuously operating, this provides quite a clear indication of the arrival of both CIR and ICME, shown in Figure 6, although this identification would be strengthened by additional plasma measurements at Venus. The regular data gaps in the magnetic field data corresponds to when Venus Express is close to the planet, at the periapsis of its elliptical orbit. Venus has no intrinsic magnetic field, but the interaction of its ionosphere with the solar wind creates an "induced magnetosphere," which has many similar features to a true magnetosphere, including bow shock followed by a magnetosheath region between the solar wind and the ionosphere [*Bertucci et al.*, 2011]. This results in sharp peaks in the magnetic field data that have been removed for clarity. The increase in magnetic field corresponding to the arrival of the CIR is slower than these regular spikes and is observed at 02:00 UT on 19 June 2010, with an associated increase in magnetic field variance in each component of the magnetic field. This indicates a compression of the magnetic field. However, this period of compressed magnetic field is very brief (lasting only 9.5 h), which is much shorter than most CIRs. It is possible that this is due to the limited measurements here, as the CIR has only been identified by its magnetic field compression. If better plasma measurements were available at Venus, they may suggest a longer CIR duration. The ENLIL-simulated total magnetic field strength is shown in Figure 6
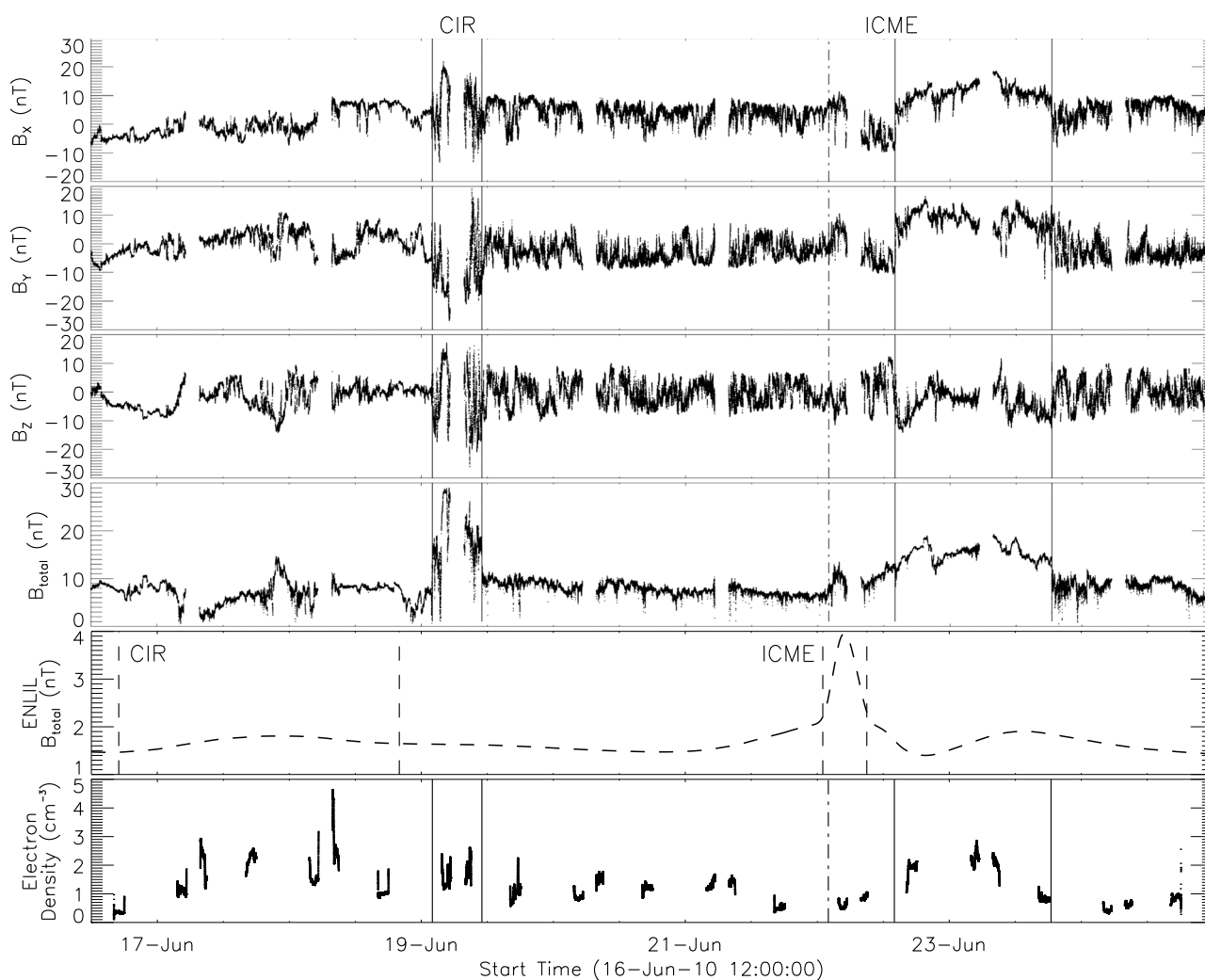
Figure 6. (first to fourth panels) The magnetic field measured by Venus Express in VSO coordinates, where *x* is positive in the direction of the Sun along the Venus-Sun line, *y* is in the orbital plane of Venus, positive in the direction opposing orbital motion, and *z* is parallel to the pole of the orbital plane and is positive in the northward direction. The periodic data gaps correspond to when Venus Express is at periapsis, close to the planet, resulting in large spikes in magnetic field which have been removed for clarity. The actual CIR and ICME intervals (02:00–11:30 UT 19 June and 14:00 UT 22 June to 18:30 UT 23 June, respectively) as suggested by the magnetic field data are indicated by the vertical lines. (fifth panel) The total magnetic field at Venus as predicted by the ENLIL model, with the dashed vertical lines indicating the predicted CIR and ICME intervals (17:00 UT 16 June to 20:00 UT 18 June and 14:00 UT 22 June to 18:80 UT 23 June, respectively). (sixth panel) The electron density as obtained from ASPERA-4 plasma moments.

(fifth panel) and shows an increase corresponding to the CIR, although it appears quite small in comparison to the much larger increase predicted for the ICME. This is the opposite of what is seen in the in situ measurements, which shows the magnetic field magnitude of the CIR to be greater than that of the ICME. In addition, the duration of the ICME predicted by ENLIL differs significantly from the in situ observations, with the observed ICME lasting over 3 times longer than predicted by ENLIL.

This figure also shows the electron density as calculated from ASPERA-4 plasma moments for the periods that it was sampling the solar wind. Plasma moments are calculated from the electron particle distribution function by integration and Gaussian fits. These are susceptible to noise but are able to show large changes and reveal the boundaries between different plasma regions. Further details of their calculation can be found in *Fränz et al.* [2006]. There are considerable data gaps, as the moments are only used when ASPERA-4 is operational in the solar wind (moments for the induced magnetosheath and ionosphere of Venus have been excluded). The first two vertical lines in Figure 6 (sixth panel) show the CIR interval suggested by the magnetic field data (when a magnetic field compression occurs), but there does not appear to be a significant increase in electron density associated with this period, though it is slightly higher than the
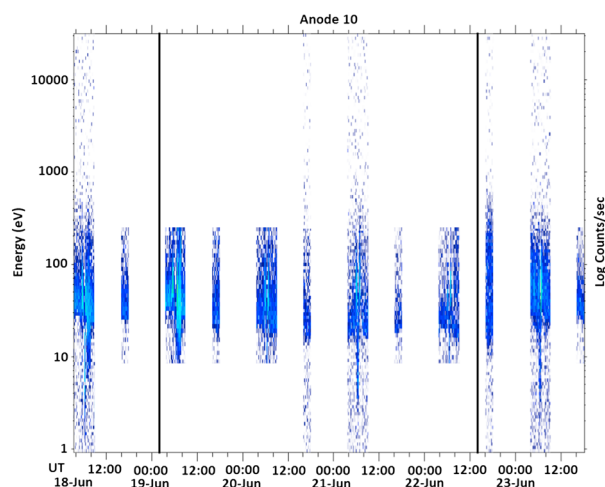
Figure 7. The ELS spectrogram for Venus Express from 18 to 23 June, covering the period when the CIR arrived (first vertical line), and the ICME arrived (second vertical line). Once a day Venus Express reaches periapsis in its orbit, passing through the induced magnetosheath region, into the ionosphere, and back out again. This is seen on the spectrogram as two regions of hot, dense electrons (the magnetosheath), bounding the cooler electrons of the ionosphere. There is an increase in the electron count rate in the solar wind and magnetosheath regions in the orbits following the arrival of the CIR and a noticeable increase in electron count rates and energy after the ICME arrival.

period following it. There is some indication of an increase in the electron density prior to the magnetic field compression, which could agree with the suggestion that the CIR duration could be longer here with plasma measurements. However, there is no reason to expect a density increase to precede the magnetic field compression rather than coinciding with it as is usual with CIRs [*Jian et al.*, 2006, 2008].

Figure 7 shows the ELS spectrogram for this period, with the CIR arrival marked by the first vertical line, as defined by the magnetic field compression. ASPERA-4 collects data twice during an orbit, once high in its orbit (sampling the solar wind), for example, from 16:03 to 17:57 UT 18 June, and once lower in the orbit, including the crossing into the induced magnetosheath and the ionosphere and back out again. This second period can be identified by the sudden increase of electron fluxes (e.g., at around 05:40 UT 18 June), corresponding to the magnetosheath

region of Venus on the inbound pass of Venus Express, followed by the ionosphere with lower electron fluxes and then a period of high electron fluxes again denoting the magnetosheath on the outbound pass of the Venus Express orbit. The figure shows that on the orbit directly following the arrival of the CIR, there is an increase in electron counts in both the solar wind and magnetosheath regions.

The ICME arrival is observed 3.5 days after the CIR (at 14:00 UT 22 June 2010), as an increase in the total magnetic field and a period of less disturbed magnetic field, in contrast to the magnetic signature of the CIR, which was a compression of the magnetic field. This period of less disturbed magnetic field is defined as the ICME interval, shown by the solid lines. There is also an increase in electron density at this time (shown in Figure 6, sixth panel), though it is possible that this electron density increase could start earlier, but it is difficult to determine with the data gaps. The increase in total magnetic field seems to begin around 12 h earlier than the period of smoother magnetic field, at 02:00 UT on 22 June (indicated by the dash-dotted vertical line), along with fluctuations in specific magnetic field directions. This is possibly a result of a solar wind pileup region or similar traveling ahead of the ICME ejecta.

ELS/ASPERA-4 spectrograms (see Figure 7) suggest an ICME arrival time consistent with the later time of 14:00 UT (second vertical line in Figure 7). ASPERA-4 is inactive from 18:01 UT 21 June to 03:49 UT 22 June and from 09:01 to 16:09 UT 22 June, over both 02:00 and 14:00 UT on 22 June. However, there is a noticeable increase in count rates of electrons at 16:09 UT, when the instrument is operating again after a break of 7 h, but there is no clear difference between 18:01 UT on 21 June and 03:48 UT on 22 June, over the previous data gap, when the solar wind pileup region possibly arrived.

3.4. The CIR and ICME at STEREO-B

At STEREO-B, both the ICME and CIR are observed, a few days after their arrival at Venus. The PLASTIC instrument allows the solar wind plasma to be sampled directly, and the magnetometer on board provides information on magnetic field variations, as shown in Figure 8. The CIR is observed to arrive at STEREO-B at 09:50 UT on 21 June 2010. As at Venus, the magnetometer observes a compression of the magnetic field, which lasts for around 20 h at STEREO-B. The plasma properties of the solar wind at STEREO-B show an increase in proton temperature, an increase and then decrease in proton density and total pressure, and a slower increase in solar wind speed. At STEREO-B, there is a small increase in density prior to the beginning
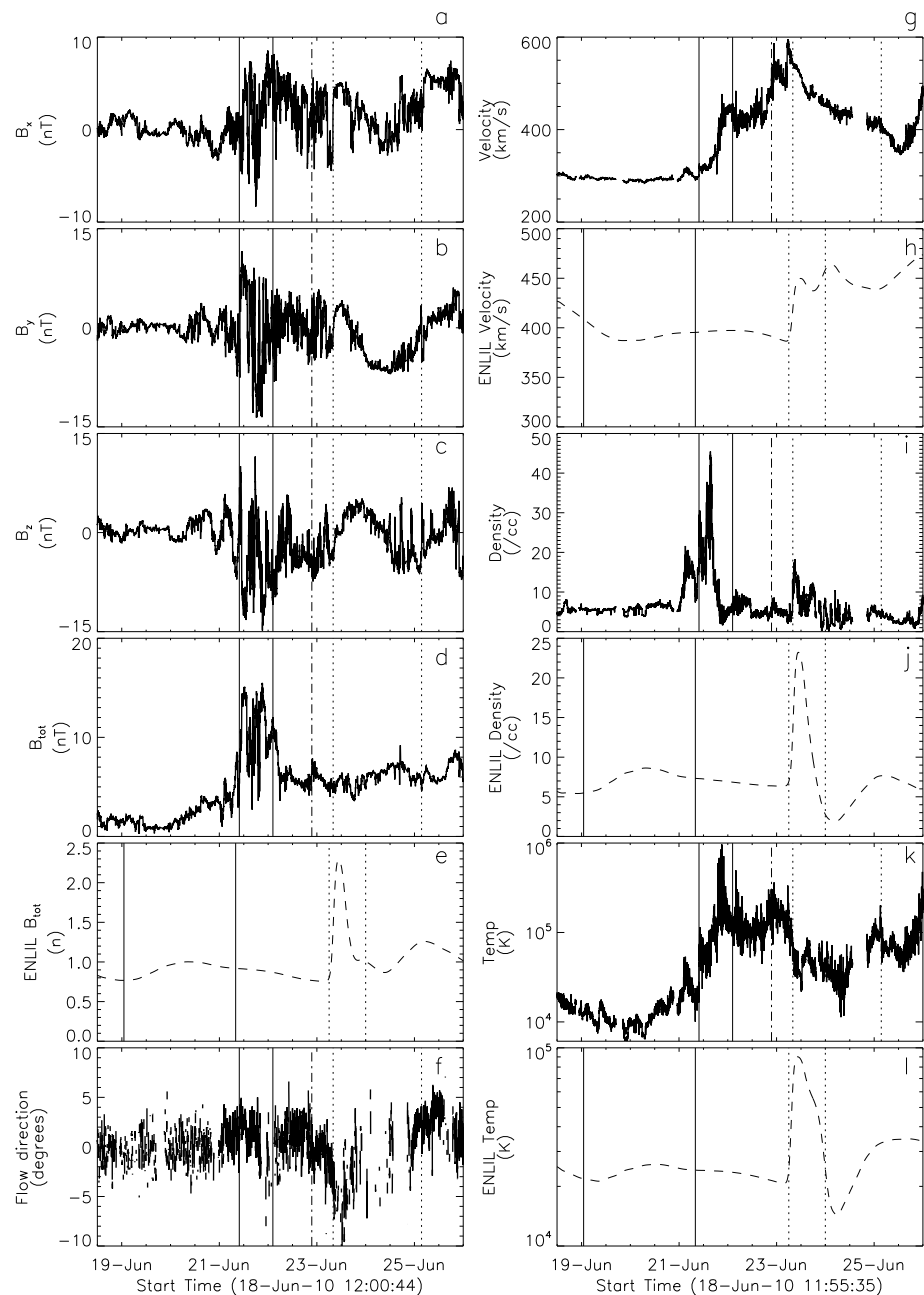
Figure 8. PLASTIC and IMPACT data of the CIR and ICME arrival at STEREO-B and ENLIL predictions. The observed and predicted CIR intervals (09:50 UT 21 June to 05:42 UT 22 June and 01:00 UT 19 June to 08:00 UT 21 June, respectively) are indicated by the solid vertical lines, and the observed and predicted ICME intervals (08:00 UT 23 June to 03:30 UT 25 June and 06:00 UT 23 June to 00:00 UT 24 June, respectively) are indicated by the dotted vertical lines. The dash-dotted line indicates the start of a possible sheath region ahead of the ICME ejecta.

of the CIR (starting early on 21 June), which may explain the possible density increase seen at Venus prior to the magnetic field compression. However, the time of this density increase is not used for the start of the CIR at STEREO-B, as the presence of several other necessary plasma characteristics seen at 09:50 UT gives a strong identification of the CIR at this later time. The ENLIL-simulated parameters are also shown in Figure 8, but as with the simulated magnetic field strength at Venus, the changes corresponding to the CIR are much smaller in comparison to the ICME. As with the results at Venus, this is generally opposite to what is seen in the in situ measurements, as the peaks of the ICME are not as high as the CIR in observations. The predicted durations of the ICME and CIR also differ from the observations, with the in situ measurements showing
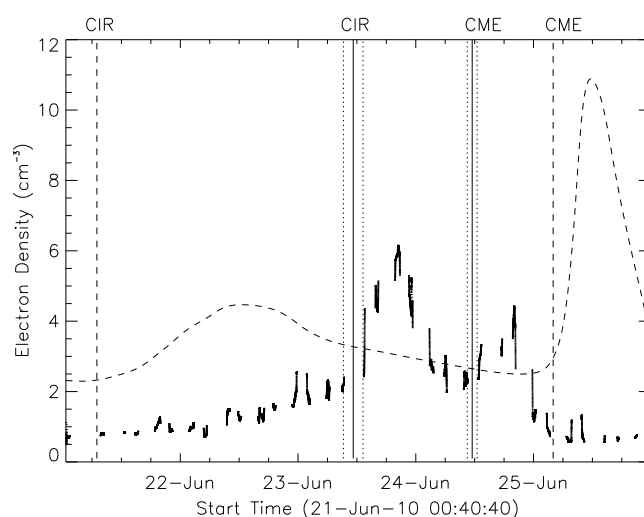
Figure 9. Electron density measured at Mars while Mars Express was in the solar wind. The start time of the CIR and the ICME (11:15 ± 02:00 UT 23 June and 11:30 ± 01:00 UT 24 June, respectively) are shown by the solid vertical lines, with the dotted lines indicating the uncertainty of these times. The overplotted dashed line shows the density as predicted by ENLIL, with the vertical dashed lines indicating the start times of the CIR and ICME (07:00 UT 21 June ad 04:00 UT 24 June, respectively).

a CIR duration of roughly 16 h and an ICME duration of roughly 42 h, compared with ENLIL simulations predicting the opposite: a CIR duration of roughly 18 h and an ICME duration of roughly 48 h.

The increase in solar wind speed associated with the CIR continues for almost 2 days, until the arrival of the ICME ejecta at 08:00 UT 23 June. The signatures of this ICME are slightly unusual at STEREO-B. A region of smooth magnetic field is evident in all three components of the magnetic field at this time, but there is no overall increase in the total magnetic field. There is an increase in proton density, not as high as that of the CIR, but little indication of an enhancement of the total pressure. The velocity of the solar wind experiences another sharp increase slightly ahead of the arrival of the ICME, which then declines steadily during CME passage.

Neither the CIR nor the ICME have interplanetary shocks associated with them at STEREO-B. Therefore, any compression region traveling ahead of the ICME ejecta (as is suggested by Figure 7) cannot be a sheath region but could be a pileup of solar wind or compression region. Despite the evidence for a possible solar wind pileup region at Venus, this region is not easy to identify in the plasma data at STEREO-B. A compression region or solar wind pileup region traveling ahead of ICME ejecta would have an increase in density and potentially a compressed magnetic field and raised temperature. The best possibility for the beginning of a compression region is marked in Figure 8 as the vertical dash-dotted line, which lies at 21:30 UT 22 June. There is no significant increase in temperature, magnetic field magnitude, or density observed, but there is a discontinuity and a small increase in these factors, and a more significant increase in solar wind velocity at this time. The magnetic field during this period remains disturbed since the earlier passage of the CIR.

3.5. The CIR and ICME at Mars

Detecting the CIR and ICME at Mars is much harder than at previous locations, as Mars Express has no magnetometer and its plasma instrument is not continuously sampling the solar wind. However, there is evidence of the arrival of two solar wind disturbances at Mars, although the timings are less reliable than those found at Venus, STEREO-B, and Earth and the identification is much less certain. Plasma moments from ASPERA-3 are shown in Figure 9 for the period 22 to 26 June, which encompasses the estimated arrival times of the ICME and CIR as given by ENLIL predictions. As with Venus, Mars has no intrinsic magnetic field but interacts with the solar wind to create an induced magnetosphere similar to that of Venus. As with Figure 6, only the moments for when ASPERA-3 is sampling the solar wind are displayed, resulting in large data gaps.

The electron density as found from plasma moments shows two peaks in density, about 1 day apart, which is less than the time between the arrival of the CIR and ICME at STEREO-B (~2 days). At STEREO-B there is a smaller density peak preceding the start of the CIR, beginning roughly 10 h earlier. However, it is unlikely that the two peaks in density seen at Mars are associated with these two peaks at STEREO-B (the main CIR and the preceding density increase). The two peaks near the CIR at STEREO-B were closer together than peaks at Mars, and the earlier peak at STEREO-B is lower than the second, opposite to what is seen at Mars. As the calculated plasma moments are susceptible to noise and only really show broad features, it seems more likely that the two density peaks observed at Mars are two distinct structures. The first density peak begins between the second and third orbits of Mars Express on 23 June 2010, which is between 09:16 UT and 13:21 UT. The arrival time of this solar wind disturbance is therefore roughly 11:15 ± 02:00 UT 23 June,
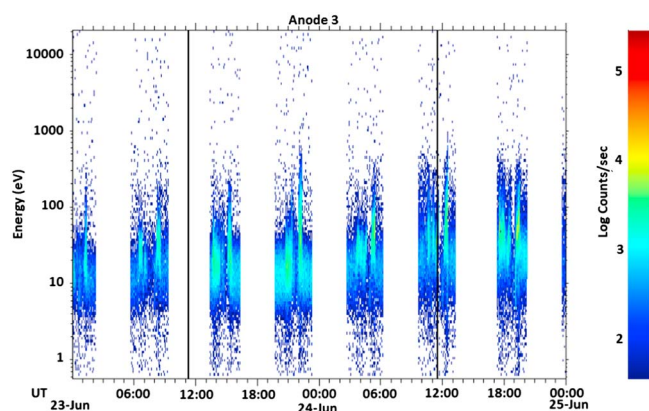
Figure 10. The ELS spectrogram for Mars Express on 23 and 24 June, covering the period when the CIR and ICME are expected to arrive at Mars. The vertical lines indicate the start time of the CIR and ICME found from the start time of the density increases seen in the plasma moments data. Mars Express carries out approximately four orbits per day, and during the periapsis of each one will pass through the induced magnetosheath of Mars, into the ionosphere, and back out through the magnetosheath. This is seen in the spectrogram as two regions of hot dense electrons corresponding to the magnetosheath, and surrounding the cooler electrons of the ionosphere. There is a clear enhancement in the electron count rate after the arrival of the CIR and in both the solar wind and magnetosheath regions, and electron energy also begins to increase at around the same time as the ICME arrival.

with the uncertainty given as the time during which no measurements are taken in the solar wind. The peak in density occurs during the inbound pass of the fourth orbit of 23 June, which is between 19:41 and 20:40 UT (within the solar wind). The second peak begins during the second orbit of 24 June, between 10:30 and 12:40 UT. The arrival of this density peak is therefore given as 11:30 $\pm$ 01:00 UT 24 June, around 1 day after the first. The peak of this density increase occurs during the outbound pass of third orbit of 24 June, corresponding to a time of roughly 20:00 UT 24 June.

The ELS spectrogram of this period is shown in Figure 10, with the start times of the two density peaks marked on as vertical lines. Similar to Venus Express spectrograms, each orbit of Mars Express includes a period close to the planet, where it crosses into the induced magnetosheath and ionosphere of the planet. This is visible in the spectrograms as two enhancements in electron count and

energy (the magnetosheath), bounding a region of cooler electrons (the ionosphere). Mars Express is only in the solar wind outside of this period. After the arrival of the first density increase (first vertical line), there is a noticeable increase in count rate of the solar wind and magnetosheath region (particularly on the outbound pass), for two orbits, until 24 June (roughly when the first density peak ends), after which the count rate is low again. At around the time of arrival of the second density increase, there is an increase in energy of solar wind electrons and the count rate is also high. The count rate and energy of the magnetosheath region also begin to increase.

The plasma moments and spectrogram data at Mars show the arrival of two solar wind disturbances here, 24 h apart. As the CIR was previously traveling ahead of the ICME, and the second density peak is lower than the first, as is the case for the CIR and ICME observed at STEREO-B, it is likely that the first density peak corresponds to the CIR and the second to the ICME. As there is only 24 h separating these two peaks in density at Mars, it suggests that the ICME is closely approaching the CIR, as it has between Venus and STEREO-B. Therefore, if these structures merge it will occur not long after the ICME has passed Mars, fairly close to the planet.

3.6. The CIR at Earth
The source location of the CME is near the center of the solar disc observed by STEREO-B (at roughly N30E90), as seen by Figure 1. Therefore, as can be seen from Figure 3, the CME is not directed toward the Earth and is not detected here. The CIR does impact the Earth almost 2.5 days after it arrives at Mars and is detected by the ACE spacecraft at L1 as seen in Figure 11. SWEPAM observes a jump in plasma density at 21:30 UT 25 June, and an increase in solar wind velocity and temperature several hours later. This is accompanied by a period of compressed magnetic field, similar to what is observed at STEREO-B and Venus, as well as an enhancement of total pressure.

3.7. The CIR in the Outer Solar System
Unlike Venus and Mars, Saturn has a strong intrinsic magnetic field, generating a true magnetosphere, similar in structure to the terrestrial magnetosphere. Cassini revolution 135 occurs around a month after the CME eruption on the Sun. The inbound part of the orbit indicates a quiet magnetosphere with regular oscillations [*Espinosa and Dougherty*, 2000, 2001; *Espinosa et al.*, 2003; *Giampieri et al.*, 2006; *Andrews et al.*,
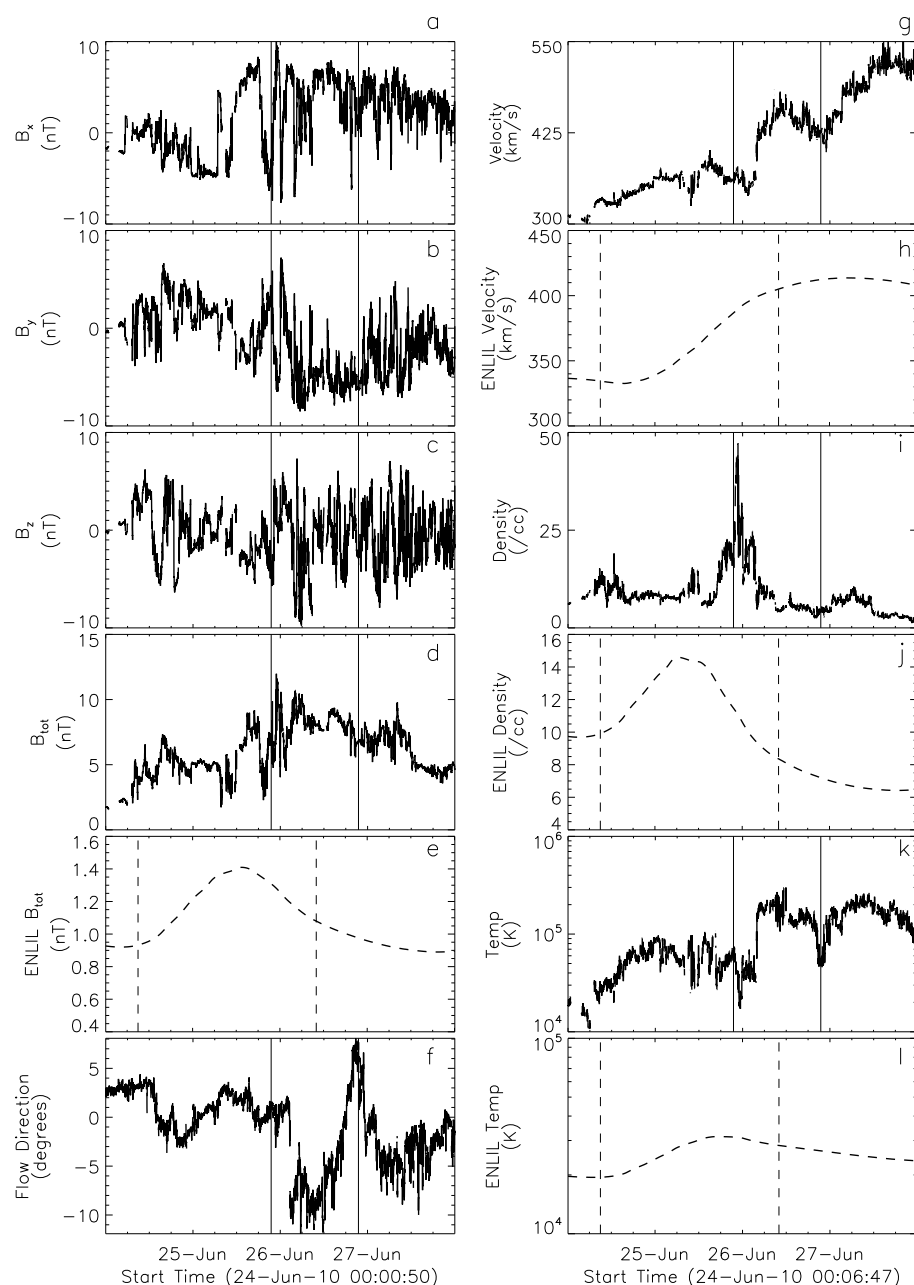
Figure 11. ACE SWEPAM data of the CIR arrival at the Earth and ENLIL predictions. The observed CIR interval (21:30 UT 25 June to 21:30 UT 26 June) is indicated by the solid vertical lines, and the predicted CIR interval (09:00 UT 24 June to 10:00 UT 26 June) are indicated by the dashed vertical lines.

2011], but the outbound pass is much more disturbed, as shown by the magnetometer data in Figure 12. On the outbound pass, Cassini first crosses the magnetopause and enters the magnetosheath of Saturn at 21:09 UT 26 July, as indicated by the decreased and disturbed region of magnetic field. For several days following this first magnetopause crossing, Cassini leaves and reenters the Saturn magnetosheath on multiple occasions, as indicated by the shaded regions of Figure 12. The final magnetopause crossing occurs at 16:05 UT on 31 July. These transitions into the magnetosheath are also observed by CAPS ELS, which sees higher density and lower temperature electrons than in the magnetosphere. These magnetopause crossings are indicative of a compression of the magnetosphere of Saturn, as Cassini has encountered the magnetosheath much closer to the planet than usual. This compression could have begun at some point while Cassini was deep in Saturn's magnetosphere (from roughly 12:00 UT 24 July) and therefore did not
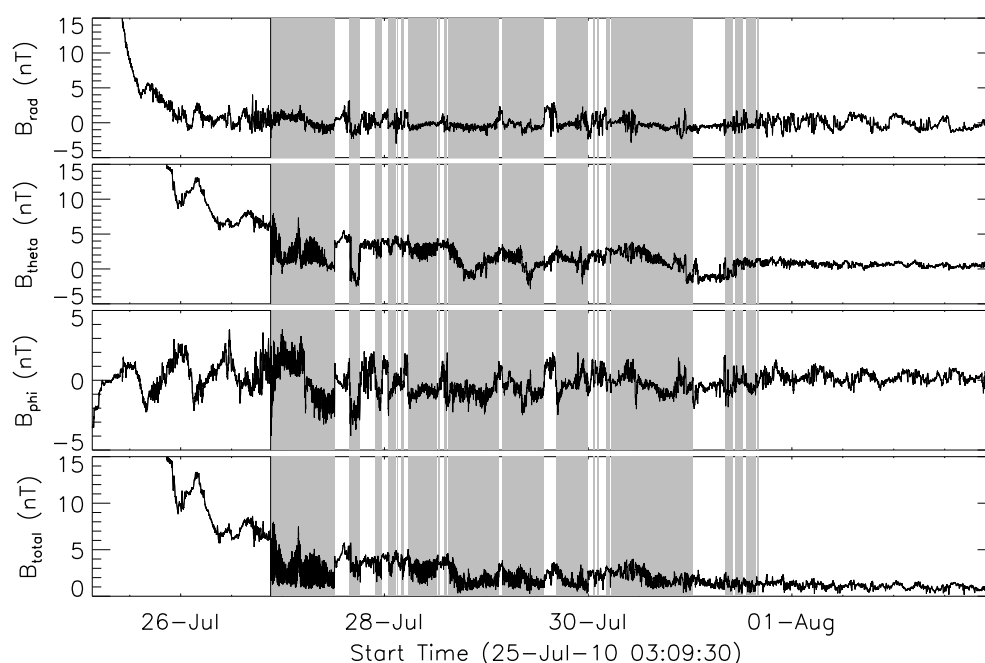
Figure 12. The magnetic field as measured by Cassini in KRTP spherical coordinates, where *r* points from Saturn to the spacecraft, phi is parallel to Saturn's equator, and theta completes the right-handed set. The shaded regions indicate the times when Cassini is within the Saturn magnetosheath, with the black vertical line showing the time of the first magnetopause crossing.

detect a change until Cassini was further from the planet (during the outbound pass), or it could have occurred at any point up until the magnetopause crossing (≈21:00 UT 26 July). The ENLIL prediction for the arrival of the CIR at Saturn is 02:00 UT 25 July, which falls within this period when a compression of the magnetosphere may have begun.

The location of the magnetopause crossings can be input to a model of the magnetopause in order to obtain an estimate of the solar wind pressure and the magnetopause standoff distance (most commonly 22 or 27 R_s, where 1 R_s = Saturn radius = 60,268 km, [*Achilleos et al.*, 2008]) at this time. The model described by *Arridge et al.* [2006] and built on by *Kanani et al.* [2010] is dependent on the pressure balance across the magnetopause boundary and uses a Newtonian form of the pressure balance equation to obtain estimates of the solar wind dynamic pressure and the standoff distance of Saturn's magnetopause. Using the first magnetopause crossing on the outbound pass (at 21:09 UT 26 July), an estimate of solar wind dynamic pressure of 0.111 nPa and a standoff distance of 16.0 R_s were found. The solar wind pressure found here is close to the pressure estimated for the CIR at Saturn as predicted by the ENLIL model, 0.107 nPa, which is over 6 times the normal solar wind pressure at this distance from the Sun. For comparison, this magnetopause model was also run for the magnetopause crossing on the inbound pass of Cassini, which occurs at 07:15 UT on 15 July. This yielded an estimate of the solar wind pressure of 0.016 nPa and an estimate of magnetopause standoff distances of 23.5 R_s. This confirms that a region of high-pressure solar wind, almost 7 times higher than the solar wind pressure during the inbound pass, has arrived at Saturn and compressed the magnetosphere significantly, by over 7 R_s. The solar wind pressure and standoff distance estimated for the final magnetopause crossing on the outbound pass (16:04 UT 31 July) were 0.012 nPa and 25.0 R_s respectively, showing that by this time the region of high-pressure solar wind has passed, and the Saturn magnetosphere has relaxed back to a less compressed state.

4. Comparison of CIR and CME Arrival Time Predictions

4.1. ENLIL Predictions
The ENLIL forecast model has provided predictions of the arrival times of both the CME and the CIR, which can be compared to the observed arrival times. These are shown in Figures 6, 8, 9, and 11, where ENLIL results are overplotted with a dashed line or plotted on a separate panel, and the timings of the CME and CIR indicated with vertical lines. These timings are summarized in Table 1, with the difference between the

Table 1. Summary of CIR and ICME Arrival Times and Predicted Arrival Times, Including Δt of the Traveling Time From Sun-Venus, Venus-STEREO-B, and STEREO-B-Mars[a]

Time of Arrival	Δt (h)	At Venus (UT)	Δt (h)	At ST-B (UT)	Δt (h)	At Mars (UT)	Δt (h)	At Earth (UT)	At Saturn (UT)
CIR		02:00 19/6	56	09:50 21/6	49.5	11:15 ± 02:00 23/6	27.5	21:30 25/6	12:00 24/7 to 21:00 26/7
ENLIL prediction		17:00 16/6 (−57 h)	56	01:00 19/6 (−57 h)	54	07:00 21/6 (−52 h)	54	09:00 24/6 (−36.5 h)	05:00 25/7
Prediction from Earth		01:30 19/6 (−0.5 h)		02:30 21/6 (−7.5 h)		02:00 23/6 (−9 h)			
Prediction from STEREO-B		05:30 19/6 (+3.5 h)				14:30 23/6 (+3.5 h)		04:30 26/6 (+7 h)	
CME	60.5	14:00 22/6	18	08:00 23/6	27.5	11:30 ± 01:00 24/6			
ENLIL prediction	48.5	02:00 22/6 (−12 h)	28.5	06:30 23/6 (−1.5 h)	48.5	07:00 25/6 (+19.5 h)			

[a]In parenthesis is given the difference between the predicted arrival time and the arrival time seen in the data.

predicted and detected arrival time given in brackets. ENLIL predicts the arrival of the CME within 20 h of the detected arrival. The prediction for the arrival at Mars is the furthest from the observed arrival: 19.5 h after it is detected by Mars Express. The closest prediction is at STEREO-B, which is 1.5 h early. The prediction for the CME arrival at Venus is 12 h early.

The ENLIL predictions of CIR arrival all show larger differences to the observed arrival times than the CME predictions, and all predict the arrival of the CIR earlier than it is detected in situ. The greatest discrepancy is seen for Venus and STEREO-B, both 2 days and 9 h too early, with the predictions then improving slightly as the CIR propagates. Repeating these predictions using alternative magnetograms or the MAS coronal model with ENLIL did not improve the timings found for the CIR arrival.

4.2. Travel Time Predictions

Williams et al. [2011] describe a method to track CIRs through the inner solar system using the speed and arrival time of the CIR detected at one location and extrapolated elsewhere. The travel time between locations, Δt, can be deduced by the simple relation:

$$\Delta t = \frac{\delta r}{V_r} + \frac{\delta \beta}{\omega_{Sun}}, \qquad (1)$$

where δr is the radial distance between the two locations, $\delta \beta$ is the angle of solar longitude between the two locations, and ω_{Sun} is the equatorial rotation rate of the Sun, 14.4° d^{-1}. V_r is the mean velocity of the CIR, calculated from the average of the minimum velocity of the low-speed stream and the maximum velocity of the high-speed stream. The method assumes that adjacent sources of fast and slow solar wind continue to emit coronal plasma at the same velocities, so that solar wind properties remain constant along a Parker field line. It also assumes that δr and $\delta \beta$ remain constant during the event, which is a reasonable approximation for the inner solar system.

This method to calculate the CIR arrivals was carried out twice; once extrapolating from the CIR detected at Earth, using V_r measured by ACE (411 km s^{-1}) and once extrapolating from STEREO-B, using V_r measured here (396 km s^{-1}). These speeds are comparable to the speed of the slow solar wind, in agreement with *Wood et al.* [2010]. This provides two arrival time predictions for Venus and Mars and one each for STEREO-B

and Earth, shown in Table 1. This method was not used to calculate the CIR's arrival at Saturn as the angle of solar longitude between each location will change significantly while the CIR propagates out to Saturn's orbit. The predictions of CIR arrival time found were all much closer to the observations than those found by the ENLIL predictions. The closest prediction was found for the arrival of the CIR at Venus, as extrapolated from the Earth, and was only half an hour early. The predicted arrival time at Mars, extrapolated from the Earth, was the furthest from its detected arrival time at 9 h early. As the Earth and Mars are the furthest apart in both longitude and radial distance at this point, it is not surprising that this prediction is the least accurate.

5. Discussion

In this study, the passage of the CIR and ICME at each location (Venus, STEREO-B, Earth, and Mars) is identified, and the events are simulated using the ENLIL prediction model. In this work, ENLIL has not been used to carry out detailed modeling of the characteristics of the CIR and ICME, but its predictions of the arrival times of these events throughout the solar system are compared with observations and also an alternative timing prediction method for the CIR. In the case of the ICME, it is important to note that as ENLIL does not simulate the internal magnetic field of the CME, what it really models is the solar wind disturbance that lies ahead of any magnetic cloud or ejecta material, which may include a shock, plasma sheath, compression region, or solar wind pileup region, although these cannot be distinguished in the model output. In this case, the ICME does not have an interplanetary shock associated with it (at least at STEREO-B, where the best plasma data are available) and so also cannot have a sheath region which lies behind an interplanetary shock. However, there was some indication of a solar wind pileup region at Venus and possibly at STEREO-B. At Mars, observations were very limited and it was impossible to draw any conclusions about the presence or timing of a solar wind pileup region associated with the ICME here. This limitation in the ENLIL model does not affect its ability to predict the arrival of a CIR at each location, however. Table 1 summarizes the arrival times of the ICME and CIR at each location and the predicted arrival times for comparison. The arrival times for the ICME at Venus and STEREO-B shown in this table correspond to the clear arrival of the ejecta, rather than any possible solar wind pileup region, which was only tentatively identified.

ENLIL predictions of the arrival times of the CIR show a significant difference to the observed arrival times at each location, with predicted times ranging from 36.5 h too early (at Earth) to 57 h too early (at Venus and STEREO-B). However, there is some sign in the electron density found from plasma moments at Venus that an increase may have begun some time earlier than the compression of the magnetic field, which would bring the arrival time of the CIR closer to that predicted by ENLIL. This discrepancy in predicted arrival times on the order of 1–2 days agrees with previous results studying ENLIL simulations of SIRs [*Jian et al.*, 2011; *Broiles et al.*, 2013] and large-scale solar wind structures [*Lee et al.*, 2009; *MacNeice et al.*, 2011; *Gressl et al.*, 2014]. An alternative method to predict the CIR arrival, described by *Williams et al.* [2011] was also assessed, finding arrival times much closer to those predicted by ENLIL. This method was a simple equation based on the corotation of the CIR but relies on data obtained as the CIR reaches one location, to extrapolate the arrival time elsewhere.

In this study, at Venus, STEREO-B, and Earth, ENLIL significantly underestimates the magnetic field strength by roughly 1 order of magnitude for the solar wind, including the ICME and CIR. This agrees broadly with the findings of *Jian et al.* [2011] and *Broiles et al.* [2013], who also find ENLIL substantially underestimates the solar wind magnetic field strength, although by not as much. The simulated temperature is also underestimated by around one order of magnitude, also in agreement with *Jian et al.* [2011], who find the temperature underestimated by about this much at 5.3 AU. The density simulated by ENLIL for the solar wind agrees with the observations fairly well at the Earth and STEREO-B, although it overestimates the peak density for the ICME and underestimates it for the CIR, which disagrees with the findings of *Jian et al.* [2011], who found that ENLIL overestimates the CIR density. At Mars the ENLIL-simulated density is overestimated for the solar wind, CIR, and ICME. The studies of *Lee et al.* [2009], *Jian et al.* [2011], and *Broiles et al.* [2013] all take place during the declining phase of solar cycle 23, whereas the events studied here occur at the beginning of cycle 24, which could have influenced the difference in the ENLIL-simulated values. The duration of the CIR as simulated by ENLIL was also overestimated, by roughly a factor of 2 at STEREO-B and Earth, which also agrees with the findings of *Jian et al.* [2011], who find CIR duration overestimated by an average factor of ~2 at 1 AU, suggesting that the model cannot simulate enough compression within 1 AU.

The arrival times of the ICME at each location as predicted by ENLIL were all closer to the detected arrival times than the CIR predictions, the largest discrepancy being for the arrival of the ICME at Mars. The ICME arrival prediction at Venus and STEREO-B were compared to the observed arrival times for the ICME ejecta given in Table 1. By instead comparing the ENLIL predictions to the arrival times of a possible solar wind pileup region, the prediction for the arrival of the ICME at Venus is much closer to observations, being only 1 h earlier than the possible solar wind pileup region at Venus (02:00 UT 22 June). At STEREO-B, however, using the arrival time of the possible solar wind pileup region for comparison worsens the ENLIL prediction here, which is now 9.5 h too early. The structure of the ICME cannot be identified at Mars, but if the timing used is only the arrival of the ICME ejecta, and a solar wind pileup region lies ahead of this, then the ENLIL prediction for Mars will show an even larger difference to the observations.

By considering the transit times of the ICME between each location in the ENLIL model (as shown in Table 1), the ICME is seen to be decelerating overall from the initial input speed of 628 km s^{-1}. This agrees with the common understanding that an ICME with an initial speed higher than that of the ambient solar wind (400 km s^{-1}) will decelerate to roughly this speed [*Gopalswamy et al.*, 2000; *Yashiro et al.*, 2004]. Similarly, an ICME traveling in faster ambient solar wind can accelerate nearly up to the speed of the ambient solar wind [*Gosling and Riley*, 1996]. Between STEREO-B and Mars, the ENLIL transit time of this ICME suggests that it has sped up again slightly. In the actual in situ measurements, the transit times of the ICME between locations differ from ENLIL predictions. It takes the ICME approximately 60 h to reach Venus (a radial distance of ≈0.7 AU), 18 h to travel between Venus and STEREO-B (a radial distance of ≈0.3 AU), and a further 28 h to reach Mars (a radial distance of ≈0.6 AU). These locations in the inner solar system are not perfectly aligned, there being 10° in longitude between Venus and STEREO-B and 8° between STEREO-B and Mars. This means that each location will encounter a different part of the curved ICME front, which will influence the observed arrival time of the ICME. As the ICME appears to be directed toward Venus (see Figure 3), STEREO-B will probably encounter the edge of the ICME, and therefore, the arrival time of the ICME here will be later than the leading front of the ICME actually reaches 1 AU. This means the transit time of the ICME between Venus and STEREO-B is longer than it would be if these spacecraft were aligned, and similarly, the transit time between STEREO-B and Mars is shorter, as Mars is only 2° away from Venus. However, this cannot account for the overall transit time between Venus and Mars (only 2° apart in longitude), which is 45.5 h. This gives an average speed of roughly 825 km s^{-1}, suggesting that the ICME is accelerating overall. This increase in velocity of the ICME has occurred despite an initial speed which is higher than the ambient solar wind speed and is also true if the possible timings of a solar wind pileup region at Venus and STEREO-B are used. This unexpected acceleration of the ICME could be due to the effect of the preceding CIR. At STEREO-B, where better plasma data are available, it can be seen that the ICME arrives during a period of high solar wind speed and lower proton density, indicating that the ICME is traveling within the high-speed solar wind stream that follows the CIR. This high-speed, low-density region could be allowing the ICME to accelerate, as the ambient solar wind at this point is at a higher velocity than that of the ICME. The average speed of the ICME during its initial propagation from the Sun to Venus is ~480 km s^{-1}, which demonstrates the expected deceleration of an ICME, and at this point the CIR is over 3 days further ahead of the ICME. It is therefore possible that the ICME propagates normally initially, decelerating as it travels into the slower ambient solar wind, until it approaches the CIR and enters the associated high-speed stream, at which point it begins to accelerate. The ENLIL model predicts that the CIR would be further ahead of the ICME, so the ICME would decelerate for longer as it propagates through the inner solar system. The ICME simulated by ENLIL only begins to show a slight acceleration while propagating between STEREO-B and Mars, when it gets closer to the CIR and its preceding high-speed solar wind stream.

The transit times of the CIR between each location are also summarized in Table 1. These give a transit time of 56 h for the CIR to travel from Venus to STEREO-B and 49.5 h to travel from STEREO-B to Mars, which seems unreasonable for a stable structure such as the CIR. However, the CIR travels in longitude as well as radially, so the fact that these locations are not exactly aligned in the inner solar system contributes significantly to the distance traveled. At this time, STEREO-B lies ~ 10° ahead of Venus in longitude and ~ 8° ahead of Mars, meaning that the CIR takes longer to travel from Venus to STEREO-B and shorter to travel from STEREO-B to Mars, than it would do if they were all in line. The equation for the transit time of a CIR, given by *Williams et al.* [2011] can be used to estimate the effect of this. The time due to the longitudinal propagation of the CIR is equal to the difference in longitude divided by the equatorial rotation rate of the Sun (14.4° day^{-1}). For Venus to STEREO-B, this corresponds to roughly 20 h and for STEREO-B to Mars, roughly 13 h.
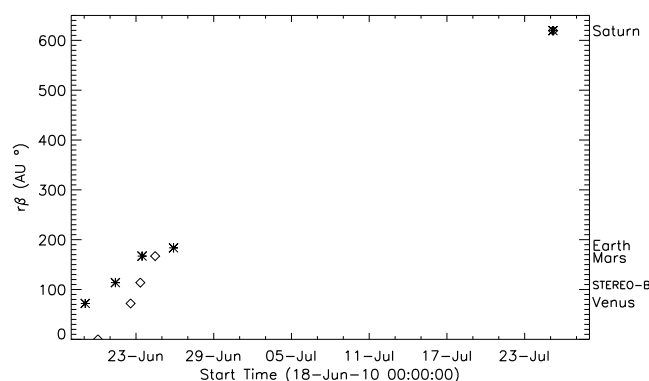
PRISE ET AL.   1583

Figure 13. A graphical representation of the timings of the CIR and CME arrivals at different locations within the solar system, where $r\beta$ is the distance from the Sun in AU multiplied by the solar longitude in degrees. The CIR is denoted by the star symbols, and the CME is denoted by the diamond symbols. The symbol at Saturn indicates that the two solar transients have merged by this point.

Therefore, if Venus, STEREO-B, and Mars were all exactly aligned in the inner solar system, and these the transit time for the CIR between them would be around 36 h between Venus and STEREO-B and 63 h between STEREO-B and Mars, which seems more reasonable.

Figure 13 gives a summary of the arrival times of these solar transients at each locations, showing the propagation of the ICME and the CIR throughout the solar system. It is clear from this that the ICME is catching up to the CIR in the inner solar system, as the overall structure of the CIR is slow in the radial direction and the ICME is traveling in the fast solar wind stream. The ICME should reach the CIR at some point beyond the orbit of Mars, before the CIR has reached the Earth (although it should be noted that it is a different part of the CIR which reaches the Earth). This is also evident from the Δt columns in Table 1, which show that the ICME is propagating faster than the CIR between each location. At Venus, the time difference between the arrival time of the CIR and CME is 84 h, decreasing to 46 h, then 24 h at STEREO-B and Mars, respectively, showing that the ICME is traveling faster than the CIR in the radial direction and will therefore eventually catch up with it. ENLIL simulation of the event indicates that when the ICME encounters the CIR, it merges with it, as shown in Figure 5, though as the simulated CIR is further ahead of the ICME, they appear to merge later, after the CIR has passed Earth.

Within the inner solar system neither the CIR or the ICME are associated with shocks, but it is likely that the pressure waves bounding the CIR will have steepened to shocks by the orbit of Saturn, as most CIRs are bounded by shocks beyond 3 AU [*Gosling and Pizzo*, 1999]. However, as Cassini is not in the solar wind at this time, there are no plasma data available to identify a shock and this cannot be verified from observations. A pressure pulse could be capable of compressing Saturn's magnetosphere, providing it is strong enough and lasts an adequately long time. Although the CIR and ICME alone are relatively small, it appears that when they merge the resulting structure has either a strong enough pressure pulse or shocks capable of strongly compressing the Saturn magnetosphere. Our observations also show that the ICME is likely to reach the CIR earlier than predicted by ENLIL, as suggested by Figure 13, which will also influence the properties of any resulting merged region as it propagates to Saturn.

While ENLIL suggests that the ICME merges with the CIR and does not reach Saturn as a distinct structure, the interaction between these two structures is unlikely to occur exactly as predicted, as the internal magnetic field of the ICME is not simulated. If the ICME does continue to travel through the outer solar system as a separate solar transient, following the interaction with the CIR, it would be very difficult to draw conclusions about its propagation beyond this point. The average ICME speed required for this to arrive while Cassini is deep in the magnetosphere of Saturn (roughly 12:00 UT 24 July to 21:00 UT 26 July), when a magnetosphere compression may have begun, is 480 km s^{-1} or lower. This is somewhat higher than the speed of the slow solar wind, which would be expected as fast ICMEs will decelerate to roughly the speed of the ambient solar wind. However, it is worth noting that this ICME is observed to accelerate during its propagation through the inner solar system, so it is possible that it would have a higher average speed during its propagation out to the orbit of Saturn. However, as the compression of the magnetosphere at Saturn is fairly strong, and the ICME is fairly weak, it seems more likely that a stronger, merged structure caused the magnetosphere compression, rather than this ICME alone.

The values of solar wind dynamic pressure and magnetopause standoff distance found from the magnetopause model of *Arridge et al.* [2006] indicate a strong compression of the Saturn magnetosphere, as the standoff distance has moved in by 7.5 R_s (1 R_s = Saturn radius = 60,268 km) and the solar wind pressure is 7 times higher. *Achilleos et al.* [2006] and *Arridge et al.* [2006] both look at several magnetopause crossings

associated with a compression of Saturn's magnetosphere and compare models of the magnetopause at this time. In general, magnetopause standoff distance is between 15 and 30 R_s and solar wind dynamic pressure is between 0.008 and 0.1 nPa, which implies that the compression seen here is strong by comparison.

6. Summary and Conclusions

This study observes two different solar transients, a CIR, followed by a ICME, as they propagate through the solar system from the Sun out to Saturn. To achieve this, it utilizes a broad range of data resources from five different spacecraft, including remote observations of the Sun, in situ solar wind measurements, various planetary spacecraft, and ENLIL prediction modeling. The CME erupted from the Sun early on 20 June 2010 and was directed roughly toward STEREO-B. The high-speed stream associated with the CIR originates from a persistent coronal hole, visible in the center of the solar disk as observed from SDO on 23 June. Signatures of these solar transients in plasma and/or magnetic data were observed at Venus, STEREO-B, and Mars and the CIR was also observed at the Earth. The in situ observations do not all yield the same parameters for easy comparison, but the timings of the transients arrivals at multiple locations have been successfully constrained, with some uncertainty, especially at Mars. The ICME does not have an interplanetary shock associated with it in the inner solar system, but a possible solar wind pileup region was identified ahead of the ICME ejecta arrival at Venus and STEREO-B. The timings of a solar wind pileup region are better compared to the ENLIL predictions. These arrival times in the inner solar system, along with ENLIL simulation of the events, indicates that the ICME eventually reaches the preceding CIR and merges with it beyond the orbit of Mars. As ENLIL does not simulate the internal magnetic field of the ICME and with actual ambient solar wind conditions likely to be different to those simulated by ENLIL, the properties of this merged interaction region cannot be determined. However, it is concluded that it is this merged structure which leads to a compression of Saturn's magnetosphere, observed by Cassini a month later. Modeling of the magnetopause of Saturn at this time suggests that this was a fairly strong compression, pushing the standoff distance in to 16.0 R_s. The ENLIL simulation of these events was not used to carry out detailed modeling of these events but to predict their arrival times at multiple locations for comparison with the observations. It was found that the predictions for the ICME were closer to the observed arrival times than those found for the CIR, which were all over a day early. This verifies earlier work which finds uncertainty in the arrival times of large-scale solar wind structures to be on the order of 1 day [*Jian et al.*, 2011; *Lee et al.*, 2009; *Gressl et al.*, 2014]. The arrival of the CIR was better predicted using the method described by *Williams et al.* [2011], which extrapolates the arrival time between locations based on the average velocity measured. The ENLIL predictions of the ICME arrival time show the ICME slowing down, as expected from a fast ICME propagating through slower ambient solar wind, whereas the observed arrival times indicate that the ICME is accelerating. This is a result of the ICME propagating through the high-speed stream of the CIR as it approaches it, allowing the ICME to accelerate. As ENLIL predicts the CIR to be traveling further ahead of the ICME (roughly 2 days earlier than observed), it shows the ICME propagating through normal, slow solar wind and therefore decelerating. This emphasizes the need for accurate simulation of the background solar wind in order to successfully model the propagation of an ICME disturbance through the solar system.

References

Achilleos, N., et al. (2006), Orientation, location, and velocity of Saturn's bow shock: Initial results from the Cassini spacecraft, *J. Geophys. Res.*, *111*, A03201, doi:10.1029/2005JA011297.

Achilleos, N., C. S. Arridge, C. Bertucci, C. M. Jackman, M. K. Dougherty, K. K. Khurana, and C. T. Russell (2008), Large-scale dynamics of Saturn's magnetosphere: Observations by Cassini, *J. Geophys. Res.*, *113*, A11209, doi:10.1029/2008JA013265.

Andrews, D. J., B. Cecconi, S. W. H. Cowley, M. K. Dougherty, L. Lamy, G. Provan, and P. Zarka (2011), Planetary period oscillations in Saturn's magnetosphere: Evidence in magnetic field phase data for rotational modulation of Saturn kilometric radiation emissions, *J. Geophys. Res.*, *116*, A09206, doi:10.1029/2011JA016636.

Arge, C. N., and V. J. Pizzo (2000), Improvement in the prediction of solar wind conditions using near-real time solar magnetic field updates, *J. Geophys. Res.*, *105*, 10,465–10,480, doi:10.1029/1999JA000262.

Arridge, C. S., N. Achilleos, M. K. Dougherty, K. K. Khurana, and C. T. Russell (2006), Modeling the size and shape of Saturn's magnetopause with variable dynamic pressure, *J. Geophys. Res.*, *111*, A11227, doi:10.1029/2005JA011574.

Baker, D. N., et al. (2009), Space environment of Mercury at the time of the first MESSENGER flyby: Solar wind and interplanetary magnetic field modeling of upstream conditions, *J. Geophys. Res.*, *114*, A10101, doi:10.1029/2009JA014287.

Baker, D. N., et al. (2011), The space environment of Mercury at the times of the second and third MESSENGER flybys, *Planet. Space Sci.*, *59*, 2066–2074, doi:10.1016/j.pss.2011.01.018.

Baker, D. N., et al. (2013), Solar wind forcing at Mercury: WSA-ENLIL model results, *J. Geophys. Res. Space Physics*, *118*, 45–57, doi:10.1029/2012JA018064.

Barabash, S., et al. (2006), The Analyzer of Space Plasmas and Energetic Atoms (ASPERA-3) for the Mars express mission, *Space Sci. Rev.*, *126*, 113–164, doi:10.1007/s11214-006-9124-8.

Barabash, S., et al. (2007), The Analyser of Space Plasmas and Energetic Atoms (ASPERA-4) for the Venus express mission, *Planet. Space Sci.*, *55*, 1772–1792, doi:10.1016/j.pss.2007.01.014.

Bertucci, C., F. Duru, N. Edberg, M. Fraenz, C. Martinecz, K. Szego, and O. Vaisberg (2011), The induced magnetospheres of Mars, Venus, and Titan, *Space Sci. Rev.*, *162*, 113–171, doi:10.1007/s11214-011-9845-1.

Broiles, T. W., M. I. Desai, C. O. Lee, and P. J. MacNeice (2013), Radial evolution of the three-dimensional structure in CIRs between Earth and Ulysses, *J. Geophys. Res. Space Physics*, *118*, 4776–4792, doi:10.1002/jgra.50482.

Brueckner, G. E., et al. (1995), The Large Angle Spectroscopic Coronagraph (LASCO), *Sol. Phys.*, *162*, 357–402, doi:10.1007/BF00733434.

Burlaga, L., D. Berdichevsky, N. Gopalswamy, R. Lepping, and T. Zurbuchen (2003), Merged interaction regions at 1 AU, *J. Geophys. Res.*, *108*(A12), 1425, doi:10.1029/2003JA010088.

Cremades, H., and V. Bothmer (2004), On the three-dimensional configuration of coronal mass ejections, *Astron. Astrophys.*, *422*, 307–322, doi:10.1051/0004-6361:20035776.

Domingo, V., B. Fleck, and A. I. Poland (1995), The SOHO Mission: An overview, *Sol. Phys.*, *162*, 1–37, doi:10.1007/BF00733425.

Dougherty, M. K., et al. (2004), The Cassini magnetic field investigation, *Space Sci. Rev.*, *114*, 331–383, doi:10.1007/s11214-004-1432-2.

Espinosa, S. A., and M. K. Dougherty (2000), Periodic perturbations in Saturn's magnetic field, *Geophys. Res. Lett.*, *27*, 2785–2788, doi:10.1029/2000GL000048.

Espinosa, S. A., and M. K. Dougherty (2001), Unexpected periodic perturbations in Saturn's magnetic field data from Pioneer 11 and Voyager 2, *Adv. Space Res.*, *28*, 919–924, doi:10.1016/S0273-1177(01)00518-X.

Espinosa, S. A., D. J. Southwood, and M. K. Dougherty (2003), Reanalysis of Saturn's magnetospheric field data view of spin-periodic perturbations, *J. Geophys. Res.*, *108*(A2), 1085, doi:10.1029/2001JA005083.

Eyles, C. J., et al. (2009), The heliospheric imagers onboard the STEREO mission, *Sol. Phys.*, *254*, 387–445, doi:10.1007/s11207-008-9299-0.

Falkenberg, T. V., B. Vršnak, A. Taktakishvili, D. Odstrcil, P. MacNeice, and M. Hesse (2010), Investigations of the sensitivity of a coronal mass ejection model (ENLIL) to solar input parameters, *Space Weather*, *8*, S06004, doi:10.1029/2009SW000555.

Falkenberg, T. V., S. Vennerstrom, D. A. Brain, G. Delory, and A. Taktakishvili (2011a), Multipoint observations of coronal mass ejection and solar energetic particle events on Mars and Earth during November 2001, *J. Geophys. Res.*, *116*, A06104, doi:10.1029/2010JA016279.

Falkenberg, T. V., A. Taktakishvili, A. Pulkkinen, S. Vennerstrom, D. Odstrcil, D. Brain, G. Delory, and D. Mitchell (2011b), Evaluating predictions of ICME arrival at Earth and Mars, *Space Weather*, *9*, S00E12, doi:10.1029/2011SW000682.

Fränz, M., E. Dubinin, E. Roussos, J. Woch, J. D. Winningham, R. Frahm, A. J. Coates, A. Fedorov, S. Barabash, and R. Lundin (2006), Plasma moments in the environment of Mars. Mars Express ASPERA-3 observations, *Space Sci. Rev.*, *126*, 165–207, doi:10.1007/s11214-006-9115-9.

Galvin, A. B., et al. (2008), The Plasma and Suprathermal Ion Composition (PLASTIC) investigation on the STEREO observatories, *Space Sci. Rev.*, *136*, 437–486, doi:10.1007/s11214-007-9296-x.

Giampieri, G., M. K. Dougherty, E. J. Smith, and C. T. Russell (2006), A regular period for Saturn's magnetic field that may track its internal rotation, *Nature*, *441*, 62–64, doi:10.1038/nature04750.

Gopalswamy, N., A. Lara, R. P. Lepping, M. L. Kaiser, D. Berdichevsky, and O. C. St. Cyr (2000), Interplanetary acceleration of coronal mass ejections, *Geophys. Res. Lett.*, *27*, 145–148, doi:10.1029/1999GL003639.

Gopalswamy, N., M. Shimojo, W. Lu, S. Yashiro, K. Shibasaki, and R. A. Howard (2003), Prominence eruptions and coronal mass ejection: A statistical study using microwave observations, *Astrophys J.*, *586*, 562–578, doi:10.1086/367614.

Gosling, J. T., and V. J. Pizzo (1999), Formation and evolution of corotating interaction regions and their three dimensional structure, *Space Sci. Rev.*, *89*, 21–52, doi:10.1023/A:1005291711900.

Gosling, J. T., and P. Riley (1996), The acceleration of slow coronal mass ejections in the high-speed solar wind, *Geophys. Res. Lett.*, *23*, 2867–2870, doi:10.1029/96GL02843.

Gosling, J. T., A. J. Hundhausen, and S. J. Bame (1976), Solar wind stream evolution at large heliocentric distances—Experimental demonstration and the test of a model, *J. Geophys. Res.*, *81*, 2111–2122, doi:10.1029/JA081i013p02111.

Gressl, C., A. M. Veronig, M. Temmer, D. Odstrčil, J. A. Linker, Z. Mikić, and P. Riley (2014), Comparative study of MHD modeling of the background solar wind, *Sol. Phys.*, *289*, 1783–1801, doi:10.1007/s11207-013-0421-6.

Gui, B., C. Shen, Y. Wang, P. Ye, J. Liu, S. Wang, and X. Zhao (2011), Quantitative analysis of CME deflections in the corona, *Sol. Phys.*, *271*, 111–139, doi:10.1007/s11207-011-9791-9.

Howard, R. A., et al. (2008), Sun Earth Connection Coronal and Heliospheric Investigation (SECCHI), *Space Sci. Rev.*, *136*, 67–115, doi:10.1007/s11214-008-9341-4.

Hundhausen, A. J., and J. T. Gosling (1976), Solar wind structure at large heliocentric distances—An interpretation of Pioneer 10 observations, *J. Geophys. Res.*, *81*, 1436–1440, doi:10.1029/JA081i007p01436.

Isavnin, A., A. Vourlidas, and E. K. J. Kilpua (2014), Three-dimensional evolution of flux-rope CMEs and its relation to the local orientation of the heliospheric current sheet, *Sol. Phys.*, *289*, 2141–2156, doi:10.1007/s11207-013-0468-4.

Jackman, C. M., N. Achilleos, E. J. Bunce, S. W. H. Cowley, M. K. Dougherty, G. H. Jones, S. E. Milan, and E. J. Smith (2004), Interplanetary magnetic field at ∼9 AU during the declining phase of the solar cycle and its implications for Saturn's magnetospheric dynamics, *J. Geophys. Res.*, *109*, A11203, doi:10.1029/2004JA010614.

Jackman, C. M., N. Achilleos, E. J. Bunce, B. Cecconi, J. T. Clarke, S. W. H. Cowley, W. S. Kurth, and P. Zarka (2005), Interplanetary conditions and magnetospheric dynamics during the Cassini orbit insertion fly-through of Saturn's magnetosphere, *J. Geophys. Res.*, *110*, A10212, doi:10.1029/2005JA011054.

Jackman, C. M., R. J. Forsyth, and M. K. Dougherty (2008), The overall configuration of the interplanetary magnetic field upstream of Saturn as revealed by Cassini observations, *J. Geophys. Res.*, *113*, A08114, doi:10.1029/2008JA013083.

Jian, L., C. T. Russell, J. G. Luhmann, and R. M. Skoug (2006), Properties of stream interactions at one AU during 1995–2004, *Sol. Phys.*, *239*, 337–392, doi:10.1007/s11207-006-0132-3.

Jian, L. K., C. T. Russell, J. G. Luhmann, R. M. Skoug, and J. T. Steinberg (2008), Stream interactions and interplanetary coronal mass ejections at 5.3 AU near the solar ecliptic plane, *Sol. Phys.*, *250*, 375–402, doi:10.1007/s11207-008-9204-x.

Jian, L. K., C. T. Russell, J. G. Luhmann, P. J. MacNeice, D. Odstrcil, P. Riley, J. A. Linker, R. M. Skoug, and J. T. Steinberg (2011), Comparison of observations at ACE and Ulysses with ENLIL model results: Stream interaction regions during Carrington rotations 2016–2018, *Sol. Phys.*, *273*, 179–203, doi:10.1007/s11207-011-9858-7.

Kanani, S. J., et al. (2010), A new form of Saturn's magnetopause using a dynamic pressure balance model, based on in situ, multi-instrument Cassini measurements, *J. Geophys. Res.*, *115*, A06207, doi:10.1029/2009JA014262.

Klein, L. W., and L. F. Burlaga (1982), Interplanetary magnetic clouds at 1 AU, *J. Geophys. Res.*, *87*, 613–624, doi:10.1029/JA087iA02p00613.

Lee, C. O., J. G. Luhmann, D. Odstrcil, P. J. MacNeice, I. de Pater, P. Riley, and C. N. Arge (2009), The solar wind at 1 AU during the declining phase of solar cycle 23: Comparison of 3D numerical model results with observations, *Sol. Phys.*, *254*, 155–183, doi:10.1007/s11207-008-9280-y.

Lemen, J. R., et al. (2012), The Atmospheric Imaging Assembly (AIA) on the Solar Dynamics Observatory (SDO), *Sol. Phys.*, *275*, 17–40, doi:10.1007/s11207-011-9776-8.

Liu, Y. D., J. D. Richardson, C. Wang, and J. G. Luhmann (2014), Propagation of the 2012 March coronal mass ejections from the Sun to heliopause, *Astrophys. J. Lett.*, *788*, L28, doi:10.1088/2041-8205/788/2/L28.

Lugaz, N., A. Vourlidas, I. I. Roussev, and H. Morgan (2009), Solar–terrestrial simulation in the STEREO Era: The 24–25 January 2007 eruptions, *Sol. Phys.*, *256*, 269–284, doi:10.1007/s11207-009-9339-4.

Lugaz, N., C. J. Farrugia, J. A. Davies, C. Möstl, C. J. Davis, I. I. Roussev, and M. Temmer (2012), The deflection of the two interacting coronal mass ejections of 2010 May 23–24 as revealed by combined in situ measurements and heliospheric imaging, *Astrophys. J.*, *759*, 68, doi:10.1088/0004-637X/759/1/68.

Luhmann, J. G., et al. (2008), STEREO IMPACT investigation goals, measurements, and data products overview, *Space Sci. Rev.*, *136*, 117–184, doi:10.1007/s11214-007-9170-x.

MacNeice, P., B. Elliott, and A. Acebal (2011), Validation of community models: 3. Tracing field lines in heliospheric models, *Space Weather*, *9*, S10003, doi:10.1029/2011SW000665.

MacQueen, R. M., A. J. Hundhausen, and C. W. Conover (1986), The propagation of coronal mass ejection transients, *J. Geophys. Res.*, *91*, 31–38, doi:10.1029/JA091iA01p00031.

McComas, D. J., S. J. Bame, P. Barker, W. C. Feldman, J. L. Phillips, P. Riley, and J. W. Griffee (1998), Solar Wind Electron Proton Alpha Monitor (SWEPAM) for the Advanced Composition Explorer, *Space Sci. Rev.*, *86*, 563–612, doi:10.1023/A:1005040232597.

Möstl, C., et al. (2012), Multi-point shock and flux rope analysis of multiple interplanetary coronal mass ejections around 2010 August 1 in the inner heliosphere, *Astrophys. J.*, *758*, 10, doi:10.1088/0004-637X/758/1/10.

Nieves-Chinchilla, T., A. Vourlidas, G. Stenborg, N. P. Savani, A. Koval, A. Szabo, and L. K. Jian (2013), Inner heliospheric evolution of a "Stealth" CME derived from multi-view imaging and multipoint in situ observations. I. Propagation to 1 AU, *Astrophys. J.*, *779*, 55, doi:10.1088/0004-637X/779/1/55.

Odstrcil, D., and V. J. Pizzo (1999), Distortion of the interplanetary magnetic field by three-dimensional propagation of coronal mass ejections in a structured solar wind, *J. Geophys. Res.*, *104*, 28,225–28,240, doi:10.1029/1999JA900319.

Odstrcil, D., and V. J. Pizzo (2009), Numerical heliospheric simulations as assisting tool for interpretation of observations by STEREO heliospheric imagers, *Sol. Phys.*, *259*, 297–309, doi:10.1007/s11207-009-9449-z.

Odstrcil, D., P. Riley, and X. P. Zhao (2004), Numerical simulation of the 12 May 1997 interplanetary CME event, *J. Geophys. Res.*, *109*, A02116, doi:10.1029/2003JA010135.

Prangé, R., L. Pallier, K. C. Hansen, R. Howard, A. Vourlidas, R. Courtin, and C. Parkinson (2004), An interplanetary shock traced by planetary auroral storms from the Sun to Saturn, *Nature*, *432*, 78–81, doi:10.1038/nature02986.

Riley, P., J. A. Linker, Z. Mikić, R. Lionello, S. A. Ledvina, and J. G. Luhmann (2006), A comparison between global solar magnetohydrodynamic and potential field source surface model results, *Astrophys. J.*, *653*, 1510–1516, doi:10.1086/508565.

Rouillard, A. P. (2011), Relating white light and in situ observations of coronal mass ejections: A review, *J. Atmos. Sol. Terr. Phys.*, *73*, 1201–1213, doi:10.1016/j.jastp.2010.08.015.

Rouillard, A. P., et al. (2009), A solar storm observed from the Sun to Venus using the STEREO, Venus Express, and MESSENGER spacecraft, *J. Geophys. Res.*, *114*, A07106, doi:10.1029/2008JA014034.

Rouillard, A. P., B. Lavraud, N. R. Sheeley, J. A. Davies, L. F. Burlaga, N. P. Savani, C. Jacquey, and R. J. Forsyth (2010), White light and in situ comparison of a forming merged interaction region, *Astrophys. J.*, *719*, 1385–1392, doi:10.1088/0004-637X/719/2/1385.

Schatten, K. H., J. M. Wilcox, and N. F. Ness (1969), A model of interplanetary and coronal magnetic fields, *Sol. Phys.*, *6*, 442–455, doi:10.1007/BF00146478.

Shen, C., Y. Wang, S. Wang, Y. Liu, R. Liu, A. Vourlidas, B. Miao, P. Ye, J. Liu, and Z. Zhou (2012), Super-elastic collision of large-scale magnetized plasmoids in the heliosphere, *Nat. Phys.*, *8*, 923–928, doi:10.1038/nphys2440.

Shen, F., C. Shen, Y. Wang, X. Feng, and C. Xiang (2013), Could the collision of CMEs in the heliosphere be super-elastic? Validation through three-dimensional simulations, *Geophys. Res. Lett.*, *40*, 1457–1461, doi:10.1002/grl.50336.

Smith, E. J., and J. H. Wolfe (1976), Observations of interaction regions and corotating shocks between one and five AU—Pioneers 10 and 11, *Geophys. Res. Lett.*, *3*, 137–140, doi:10.1029/GL003i003p00137.

Taktakishvili, A., M. Kuznetsova, P. MacNeice, M. Hesse, L. Rastätter, A. Pulkkinen, A. Chulaki, and D. Odstrcil (2009), Validation of the coronal mass ejection predictions at the Earth orbit estimated by ENLIL heliosphere cone model, *Space Weather*, *7*, S03004, doi:10.1029/2008SW000448.

Thompson, W. T., et al. (2003), COR1 inner coronagraph for STEREO-SECCHI, in *Soc. Photo-Optical Instrument. Eng. (SPIE) Conf. Ser. 4853*, edited by S. L. Keil and S. V. Avakyan, pp. 1–11, SPIE, Bellingham.

Vršnak, B., M. Temmer, T. Žic, A. Taktakishvili, M. Dumbović, C. Möstl, A. M. Veronig, M. L. Mays, and D. Odstrčil (2014), Heliospheric propagation of coronal mass ejections: Comparison of numerical WSA-ENLIL+Cone model and analytical drag-based model, *Astrophys. J. Suppl. Ser.*, *213*, 21, doi:10.1088/0067-0049/213/2/21.

Wang, Y., C. Shen, S. Wang, and P. Ye (2004), Deflection of coronal mass ejection in the interplanetary medium, *Sol. Phys.*, *222*, 329–343, doi:10.1023/B:SOLA.0000043576.21942.aa.

Wang, Y., H. Zheng, S. Wang, and P. Ye (2005), MHD simulation of the formation and propagation of multiple magnetic clouds in the heliosphere, *Astron. Astrophys.*, *434*, 309–316, doi:10.1051/0004-6361:20041423.

Wang, Y., C. Chen, B. Gui, C. Shen, P. Ye, and S. Wang (2011), Statistical study of coronal mass ejection source locations: Understanding CMEs viewed in coronagraphs, *J. Geophys. Res.*, *116*, A04104, doi:10.1029/2010JA016101.

Wang, Y., B. Wang, C. Shen, F. Shen, and N. Lugaz (2014), Deflected propagation of a coronal mass ejection from the corona to interplanetary space, *J. Geophys. Res. Space Physics*, *119*, 5117–5132, doi:10.1002/2013JA019537.

Wang, Y. M., P. Z. Ye, and S. Wang (2003), Multiple magnetic clouds: Several examples during March-April 2001, *J. Geophys. Res*, *108*(A10), 1370, doi:10.1029/2003JA009850.

Webb, D. F., T. A. Howard, C. D. Fry, T. A. Kuchar, D. Odstrcil, B. V. Jackson, M. M. Bisi, R. A. Harrison, J. S. Morrill, R. A. Howard, and J. C. Johnston (2009), Study of CME propagation in the inner heliosphere: SOHO LASCO, SMEI and STEREO HI observations of the January 2007 events, *Sol. Phys.*, *256*, 239–267, doi:10.1007/s11207-009-9351-8.

Williams, A. O., N. J. T. Edberg, S. E. Milan, M. Lester, M. Fränz, and J. A. Davies (2011), Tracking corotating interaction regions from the Sun through to the orbit of Mars using ACE, MEX, VEX, and STEREO, *J. Geophys. Res.*, *116*, A08103, doi:10.1029/2010JA015719.

Wood, B. E., R. A. Howard, A. Thernisien, and D. G. Socker (2010), The three-dimensional morphology of a corotating interaction region in the inner heliosphere, *Astrophys. J. Lett.*, *708*, L89–L94, doi:10.1088/2041-8205/708/2/L89.

Wood, B. E., C.-C. Wu, A. P. Rouillard, R. A. Howard, and D. G. Socker (2012), A coronal hole's effects on coronal mass ejection shock morphology in the inner heliosphere, *Astrophys. J.*, *755*, 43, doi:10.1088/0004-637X/755/1/43.

Wu, C.-C., C. D. Fry, M. Dryer, S. T. Wu, B. Thompson, K. Liou, and X. S. Feng (2007), Three-dimensional global simulation of multiple ICMEs' interaction and propagation from the Sun to the heliosphere following the 25–28 October 2003 solar events, *Adv. Space Res.*, *40*, 1827–1834, doi:10.1016/j.asr.2007.06.025.

Wu, C.-C., M. Dryer, S. T. Wu, B. E. Wood, C. D. Fry, K. Liou, and S. Plunkett (2011), Global three-dimensional simulation of the interplanetary evolution of the observed geoeffective coronal mass ejection during the epoch 1–4 August 2010, *J. Geophys. Res.*, *116*, A12103, doi:10.1029/2011JA016947.

Wu, C.-C., K. Liou, S. T. Wu, M. Dryer, C. D. Fry, and S. Plunkett (2012), Heliospheric three-dimensional global simulation of multiple interacting coronal mass ejections during the Halloween 2003 epoch, *AIP Conf. Proc.*, *1436*(1), 285–291, doi:10.1063/1.4723621.

Wu, S. T., C. Wu, K. Liou, S. Plunkett, M. Dryer, and C. D. Fry (2014), Analyses of the evolution and interaction of multiple coronal mass ejections and their shocks in July 2012, *Astron. Soc. Pacific Conf. Ser.*, vol. 484, edited by Q. Hu and G. P. Zank, p. 241, Astronomical Society of the Pacific, San Francisco, Calif.

Wuelser, J.-P., et al. (2004), EUVI: The STEREO-SECCHI extreme ultraviolet imager, *Proc. SPIE*, *5171*, 111–122, doi:10.1117/12.506877.

Xiong, M., H. Zheng, S. T. Wu, Y. Wang, and S. Wang (2007), Magnetohydrodynamic simulation of the interaction between two interplanetary magnetic clouds and its consequent geoeffectiveness, *J. Geophys. Res.*, *112*, A11103, doi:10.1029/2007JA012320.

Yashiro, S., N. Gopalswamy, G. Michalek, O. C. St. Cyr, S. P. Plunkett, N. B. Rich, and R. A. Howard (2004), A catalog of white light coronal mass ejections observed by the SOHO spacecraft, *J. Geophys. Res.*, *109*, A07105, doi:10.1029/2003JA010282.

Young, D. T., et al. (2004), Cassini plasma spectrometer investigation, *Space Sci. Rev.*, *114*, 1–112, doi:10.1007/s11214-004-1406-4.

Zhang, T. L., et al. (2006), Magnetic field investigation of the Venus plasma environment: Expected new results from Venus Express, *Planet. Space Sci.*, *54*, 1336–1343, doi:10.1016/j.pss.2006.04.018.

Zurbuchen, T. H., and I. G. Richardson (2006), In-situ solar wind and magnetic field signatures of interplanetary coronal mass ejections, *Space Sci. Rev.*, *123*, 31–43, doi:10.1007/s11214-006-9010-4.